FIRST-PRINCIPLES STUDY OF CPP GMR IN Co/Cu MULTILAYERS INCLUDING SUBSTITUTIONAL DISORDER AND SPIN-ORBIT COUPLING

UNIVERSITY OF TWENTE.

H. L. DAO

A thesis submitted for the degree of

MASTER OF APPLIED PHYSICS

2012

Contents

Chapter 1

Introduction

The field of spintronics (spin-polarized transport) has come a long way since the discovery of Giant Magnetoresistance (GMR) effect independently by A. Fert and P. Grunberg in the 80s, which triggered both scientific and commercial interests eversince. Early experimental studies of GMR effect mostly used the Current-In-Plane (CIP) geometry due to the ease of measurement compared to the Current-Perpendicular-to-Plane (CPP) geometry (CIP has larger and more measurable resistances of the order $10^{-2}\,\Omega$ or greater, while CPP resistance of the order $10^{-8}\,\Omega$ [1] is much smaller and harder to measure [1]). However, it is difficult in CIP studies to separately quantify spin-polarized bulk and interface-dependent electron scattering within the multilayer while just the opposite is true in CPP case. Moreover, CPP-GMR has been experimentally and theoretically confirmed to be several times larger than CIP-GMR. This, and the fact that fundamental parameters are more accessible in CPP-GMR lead to more and more studies of CPP-GMR.

The first experimental studies of CPP-GMR were published in 1991 by the group of J. Bass and W. P. Pratt Jr. in Michigan State University (MSU) [2], and together with that, the introduction of the phenomenological Two-Current-Series Resistor (2CSR) model - a straightforward way of extracting relevant parameters pertaining to spin transport in CPP geometry. The 2CSR model states that (in CPP structure) with no spin-flip scattering allowed, we have two independent current-carrying channels due to the two different spin states, and as long as the transport is completely diffusive, the spin-dependent scattering of each spin channel within the bulk layers and at the interfaces are assumed to be resistive components added in series. At low temperature, spin flip scattering by magnons and phonons is negligible, and the only mechanism capable of mixing the two spin channels is spin orbit coupling (SOC). It is therefore

of fundamental interests to study the effect of SOC on CPP-GMR, to explore the validity of the 2CSR in general and especially in the presence of SOC. In this perspective, this Master project is primarily a first-principles study of SOC's influence on CPP-GMR and its fundamental parameters. To achieve a more complete understanding, the influence of substitutional disorder in the ferromagnetic (Co) layers in CPP structure on CPP-GMR was also studied. The obtained calculations' results are then compared with the published CPP experimental results of the MSU group (extracted using the 2CSR Model).

An overview of the theoretical aspects and methods is presented in Chapter 2, followed by a review of the experimental characterization of the CPP multilayered samples and the 2CSR Model in Chapter 3. Finally, the calculations' results are presented and discussed in Chapter 4. Appendix A gives an overview of the basic physics of X-ray diffraction and possible defects associated with the broadening of the X-ray diffraction peaks. Appendix B gives a one-dimensional quantum mechanical description of a spin-dependent coherent versus incoherent tranport using the double square potentiel barrier model.

Chapter 2

Theory and Methods

2.1 Density Functional Theory

The essential idea of Density Functional Theory (DFT) is that the complicated many-body problem is reduced by an effective single particle theory. [3]

The Hamiltonian for N interacting electrons is given as:

$$H = T + V + U, \tag{2.1}$$

where the corresponding terms are:

T - the kinetic energy:

$$T = -\sum_{i=1}^{N} \nabla_i^2. \tag{2.2}$$

V - the external potential (according to Bohn-Oppenheimer, V consists of the potential due to the static ions located at fixed position $\mathbf{R}_\mu$ and other external fields - $v_{field}(\mathbf{r})$)

$$V = \sum_{i=1}^{N} v_{ext}(\mathbf{r}_i) = \sum_{i=1}^{N} \left(\sum_{\mu} v_{ion}(\mathbf{r} - \mathbf{R}_\mu) + v_{field}(\mathbf{r}) \right). \tag{2.3}$$

U - the electron-electron Coulomb interaction:

$$V = \sum_{i,j} \frac{1}{|\mathbf{r}_i - \mathbf{r}_j|}. \tag{2.4}$$

Defining the electron-density operator:

$$\hat{n}(\mathbf{r}) = \sum_{i=1}^{N} \delta(\mathbf{r} - \mathbf{r}_i), \tag{2.5}$$

from which the electron density is the eigenvalue of the electron-density operator:

$$n(\mathbf{r}) = \langle\psi|\hat{n}(\mathbf{r})|\psi\rangle. \tag{2.6}$$

The Hohenberg and Kohn theorem states that :

1. The total ground state energy, E, of any many-electron system is a functional of the density $n(\mathbf{r})$:
$$E[n] \;=\; F[n] \;+\; \int n(\mathbf{r})v_{ext}(\mathbf{r})d\mathbf{r}, \tag{2.7}$$
where $F[n]$ is also a functional of the density $n(r)$ but independent of the external potential.

2. For any many-electron system the functional $E[n]$ for the total energy has a minimum equal to the ground-state energy at the ground-state density

Following Kohn and Sham (1965), who derived the single-particle Schrodinger equation using the variational principle implied by the minimal properties of the energy functional, we start by defining the functional $F[n]$:

$$F[n] \;=\; T[n] \;+\; \int\int \frac{n(\mathbf{r})n(\mathbf{r}')}{|\mathbf{r} \;-\; \mathbf{r}'|}d\mathbf{r}' \;+\; E_{xc}[n], \tag{2.8}$$

where the first, second, and third term of (2.8) are the kinetic, Hartree, and exchange-correlation energy, respectively.

Splitting the kinetic energy term into two component: T_0 (the kinetic energy of noninteracting particles) and T_{xc} (accounting for the rest), we have:

$$T \;=\; T_0 \;+\; T_{xc}, \tag{2.9}$$

With:

$$n(\mathbf{r}) \;=\; \sum_{i\,=\,1}^{N} |\phi_i(\mathbf{r})|^2, \tag{2.10}$$

and:

$$T_0[n] \;=\; \sum_{i\,=\,1}^{N} \int \nabla\phi_i^*(\mathbf{r})\nabla\phi_i(\mathbf{r}), \tag{2.11}$$

where ϕ is the single-particle wavefunction.
From (2.7), (2.8), and (2.9) we have:

$$E[n] \;=\; T_0[n] \;+\; T_{xc}[n] \;+\; E_{xc}[n] \;+\; \int\int \frac{n(\mathbf{r})n(\mathbf{r}')}{|\mathbf{r} \;-\; \mathbf{r}'|}d\mathbf{r}' \;+\; \int n(\mathbf{r})v_{ext}(\mathbf{r})d\mathbf{r}, \tag{2.12}$$

one has the following postulate:

$$\left(-\nabla^2 + v_{eff}(\mathbf{r})\right)\phi_i(\mathbf{r}) = \epsilon_i\phi_i(\mathbf{r}), \tag{2.13}$$

Left-multiplying (2.13) with ϕ_r^* and requiring that ϕ_r be normalized, then integrating and summing up one has:

$$T_0[n] = \sum_{i=1}^{N}\epsilon_i - \int v_{eff}(\mathbf{r})n(\mathbf{r})d(\mathbf{r}), \tag{2.14}$$

$v_{eff}(\mathbf{r})$ is the potential to be determined such that the density $n(\mathbf{r})$ obtained from (2.9) minimizes the total energy.

Using the variational procedure :

$$\frac{\delta E[n]}{\delta n(\mathbf{r})} + \frac{\mu\delta[N - \int n(\mathbf{r})d(\mathbf{r})]}{\delta n(\mathbf{r})}, \tag{2.15}$$

one has:

$$v_{eff}(\mathbf{r}) = v_{ext}(\mathbf{r}) + 2\int\frac{n(\mathbf{r}')}{|\mathbf{r}-\mathbf{r}'|}d\mathbf{r}' + v_{xc}(\mathbf{r}), \tag{2.16}$$

with :

$$v_{xc}(\mathbf{r}) = \frac{\partial(E_{xc} + T_{xc})}{\partial n(\mathbf{r})}. \tag{2.17}$$

The effective single-particle equation:

$$\left(-\nabla^2 + v_{eff}(\mathbf{r}) - \epsilon_i\right)\phi_i(\mathbf{r}) = 0, \tag{2.18}$$

is the Kohn-Sham (KS) equation, in which the external potential is replaced by the effective potential which depends on the density $n(\mathbf{r})$, which itself depends on the single-particle wavefunction ϕ_i. Hence, the KS equation effectively constitutes a self-consistent problem.

The total ground state energy as a functional of the density can be determined from (2.12) and (2.14):

$$\begin{aligned} E[n] &= \left\{\sum_{i=1}^{N}\epsilon_i - \int v_{eff}(\mathbf{r})n(\mathbf{r})d(\mathbf{r})\right\} + T_{xc}[n] + E_{xc}[n] \\ &+ \int\int\frac{n(\mathbf{r})n(\mathbf{r}')}{|\mathbf{r}-\mathbf{r}'|}d\mathbf{r}' + \int n(\mathbf{r})v_{ext}(\mathbf{r})d\mathbf{r} \end{aligned} \tag{2.19}$$

From (2.16), (2.19) becomes:

$$\boxed{E[n] = \sum_{i=1}^{N}\epsilon_i - \int\int\frac{n(\mathbf{r})n(\mathbf{r}')}{|\mathbf{r}-\mathbf{r}'|}d\mathbf{r}' - \int v_{xc}(\mathbf{r})n(\mathbf{r})d(\mathbf{r}) + \tilde{E}_{xc}[n]} \tag{2.20}$$

where $\tilde{E}_{xc}[n] = E_{xc}[n] + T_{xc}[n]$.

The DFT can be generalized to the spin-polarized case (Spin Density Functional Theory, SDFT), in which the density is replaced by a density matrix (in the case where the spin state cannot be described by a single, global quantization axis) $n_{\beta\alpha}(\mathbf{r})$ (β, α are spin indices)

The expression for the total energy in SDFT is similar to that of DFT:

$$\boxed{E[\tilde{n}] = \sum_{i=1}^{N} \epsilon_i - \int\int \frac{n(\mathbf{r})n(\mathbf{r}')}{|\mathbf{r} - \mathbf{r}'|} d\mathbf{r}' - \sum_{\alpha\beta} \int v^{xc}_{\alpha\beta}(\mathbf{r}) n_{\beta\alpha}(\mathbf{r}) d(\mathbf{r}) + \tilde{E}_{xc}[\tilde{n}]}, \tag{2.21}$$

2.2 Local Spin Density Approximation

In the Local Density Approximation (LDA), the homogeneous, interacting electron gas serves to model the exchange-correlation energy in the form:

$$\tilde{E}_{xc}[n] = \int n(\mathbf{r}) \epsilon_{xc}(n(\mathbf{r})) d(\mathbf{r}). \tag{2.22}$$

$\epsilon_{xc}(n(\mathbf{r}))$ is a function of the density $n(\mathbf{r})$. Eq.(2.22) can be viewed as approximating an inhomogeneous electron gas by many 'local' volumes (positioned at $\mathbf{r}$) of small, homogeneous interacting electron gas with density $n(\mathbf{r})$.

The exchange-correlation potential is:

$$v_{xc}(\mathbf{r}) = \left[\frac{d}{dn} \{ n\epsilon_{xc}(n) \} \right]_{n = n(\mathbf{r})}. \tag{2.23}$$

The LDA can be generalized to the spin-polarized case, assuming the eigenvalues of the density matrix to be $n_\uparrow(\mathbf{r})$ and $n_\downarrow(\mathbf{r})$, the exchange-correlation energy is :

$$E_{xc}[\tilde{n}] = \int n(\mathbf{r}) \epsilon_{xc}(n_\uparrow(\mathbf{r}), n_\downarrow(\mathbf{r})) d(\mathbf{r}). \tag{2.24}$$

The exchange-correlation potential is:

$$v^{xc}_{\alpha}(\mathbf{r}) = \left[\frac{\partial}{\partial n_\alpha} \{ n\epsilon_{xc}(n_\uparrow, n_\downarrow) \} \right]_{n_\uparrow = n_\uparrow(\mathbf{r}), n_\downarrow = n_\downarrow(\mathbf{r})}. \tag{2.25}$$

where $\alpha = \uparrow$ or $\downarrow$.

2.3 Linear Muffin Tin Orbitals Basis Set

2.3.1 Muffin Tin Orbitals and the Tail-Cancellation Condition

Starting with the effective one-electron Schrodinger equation [4]:

$$(-\nabla^2 + V(r) - E)\Psi = 0, \tag{2.26}$$

for which the potential V(r) is taken to be spherically symmetric within regions of space known as atomic spheres and constant with value V_0 in the interstitial region outside the spheres.

2.3.1.1 Interstitial region

In the interstitial region the wavefunction Ψ satisfies the Laplace equation $\nabla^2\Psi = 0$ and it is a linear superposition of the solutions $J_L(r)$ and $K_L(r)$ of the Laplace equation.

$$\begin{aligned} J_L(r) &= J_l(r)Y_L(\hat{r}) \\ K_L(r) &= K_l(r)Y_L(\hat{r}) \end{aligned}$$

$$J_l(r) = \frac{1}{2(2l+1)}\left(\frac{r}{w}\right)^l, \tag{2.27}$$

$$K_l(r) = \left(\frac{w}{r}\right)^{l+1}. \tag{2.28}$$

In the interstitial region, $J_L(r)$ is the irregular solution (diverges as $r \to +\infty$) and $K_L(r)$ is the regular solution (vanishes as $r \to +\infty$). However, inside atomic spheres, $K_L(r)$ is irregular (diverges as $r \to 0$) and $J_L(r)$ is regular (vanishes as $r \to 0$).

Furthermore, one can expand $K_L(r_R)$ (irregular solution of Laplace equation inside an atomic sphere centered at R) in terms of $J_L(r_R)$ (regular solution of Laplace equation in atomic spheres centered at R' - $R' \neq R$) as:

$$K_L(r_R) = -\sum_{L'} S_{\mathbf{R}L,\mathbf{R}'L'} J_{L'}(r_{\mathbf{R}'}). \tag{2.29}$$

$S_{\mathbf{R}L,\mathbf{R}'L'}$ is called the canonical structure constant.

2.3.1.2 Single Site Problem

Supposing there is only one sphere in all space - Within that particular atomic sphere the wavefunction Ψ satisfies the radial Schrodinger equation:

$$\left(-\frac{\partial^2}{\partial r^2} - \frac{2}{r}\frac{\partial}{\partial r} + v\frac{l(l+1)}{r^2} + V_{\mathbf{R}}(r) - E\right)\varphi_{\mathbf{R}L}(r,E) = 0, \tag{2.30}$$

$$\Psi = \varphi_{\mathbf{R}L}(r,E) = \varphi_{\mathbf{R}l}(r,E)Y_L(\hat{r}). \tag{2.31}$$

There are 2 solutions to the radial Schrodinger equation, given approximately as:

$$\varphi_{\mathbf{R}l} \sim r^l, \tag{2.32}$$

$$\varphi_{\mathbf{R}l} \sim r^{-l-1}. \tag{2.33}$$

The wavefunction in all space is constructed by requiring the continuity of the wavefunction (and their derivatives) at the sphere boundary (separating the space within the sphere and the interstial region).

Defining the logarithmic derivative as:

$$D[f(r)] = \frac{\partial lnf(r)}{\partial lnr} = r\frac{f'(r)}{f(r)}, \tag{2.34}$$

with $f'(r) = \frac{df(r)}{dr}$.

The logarithmic derivatives of $J_l(r)$, $K_l(r)$ and φ_{Rl} at the sphere boundary $r = s_R$ are:

$$\begin{aligned} D[J_l(r)] &= l, \\ D[K_l(r)] &= -l - 1, \\ D[\varphi_{\mathbf{R}l}(r,E)] &= D_{\mathbf{R}l}(E) \end{aligned}$$

Considering the Wronskian of 2 functions $f_1(r)$ and $f_2(r)$:

$$\begin{aligned} \{f_1(r), f_2(r)\} &= r^2[f_1(r)f_2'(r) - f_1'(r)f_2(r)] \\ &= r^2 f_1(r)f_2(r)\,(D[f_2(r)] - D[f_1(r)]) \end{aligned}$$

One uses the Wronskian to match a function f(r) continuously into a linear superposition of 2 other functions $f_1(r)$ and $f_2(r)$ as:

$$f(r) \to \frac{\{f, f_2\}f_1(r) - \{f, f_1\}f_2(r)}{\{f_1, f_2\}}. \tag{2.35}$$

For $J_l(r)$ and $K_l(r)$, the Wronskian is:

$$\{J_l(r),\, K_l(r)\} = -\frac{w}{2}. \tag{2.36}$$

Applying the matching condition (2.35) at $r = s_R$ to this case to match $\varphi_{Rl}(r,E)$ to a linear combination of $J_l(r)$ and $K_l(r)$:

$$\varphi_{\mathbf{R}l}(r,E) \to \frac{2}{w}\left[\{\varphi_{Rl}(r,E), J_l(r)\}K_l(r) - \{\varphi_{\mathbf{R}l}(r,E), K_l(r)\}J_l(r)\right]. \tag{2.37}$$

Defining:

$$P_{\mathbf{R}l}(E) = \frac{\{K_l(r), \varphi_{\mathbf{R}l}(r,E)\}}{\{J_l(r), \varphi_{\mathbf{R}l}(r,E)\}}|r = s_{\mathbf{R}} \tag{2.38}$$

and:

$$N_{\mathbf{R}l}(E) = \frac{w}{2}\frac{1}{\{\varphi_{\mathbf{R}l}(r,E), J_l(r)\}}|r = s_{\mathbf{R}}. \tag{2.39}$$

Using (2.38) and (2.39), (2.37) becomes:

$$N_{\mathbf{R}l}(E)\varphi_{\mathbf{R}l}(r,E) \to K_l(r) - P_{\mathbf{R}l}(E)J_l(r). \tag{2.40}$$

2.3.1.3 The Tail Cancellation Condition

The real problem is solving (2.26) for the case of multiple spheres using the muffin-tin orbital basis:

$$\psi_{\mathbf{R}L}(r,E) = \begin{cases} N_{\mathbf{R}l}(E)\psi_{\mathbf{R}l}(r_{\mathbf{R}},E) + P_{\mathbf{R}l}(E)J_L(r_{\mathbf{R}}) & (r_{\mathbf{R}} \leq s_{\mathbf{R}}) \\ K_L(r_{\mathbf{R}}) & (r_{\mathbf{R}} \geq s_{\mathbf{R}}). \end{cases} \tag{2.41}$$

The trial wavefunction is then

$$\psi(r) = \sum_{\mathbf{R}L} a_{\mathbf{R}L}\psi_{\mathbf{R}L}(r,E). \tag{2.42}$$

(2.41) satisfies the Laplace equation outside its own sphere (the sphere centered at $\mathbf{R}$) but does not satisfy the Schrodinger Equation (2.26) in its own atomic sphere. In order for (2.41) to satisfy the Schrodinger equation in its own sphere (centered at R), the tail equation $K_L(r)$ is expanded into a linear combination of $J_{L'}(r_{\mathbf{R}'})$ in other spheres centered at R' Substituting (2.51) into (2.42), one has the Schrodinger Equation (2.26) satisfy inside the sphere centered at R, and also in R' if:

$$\boxed{\sum_{\mathbf{R}L} a_{\mathbf{R}L}[P_{\mathbf{R}l}(E)\delta_{\mathbf{R}L,\mathbf{R}'L'} - S_{\mathbf{R}L,\mathbf{R}'L'}] = 0}. \tag{2.43}$$

Non-trivial solution exists if:

$$\boxed{det(P_{\mathbf{R}l}(E)\delta_{\mathbf{R}L,\mathbf{R}'L'} - S_{\mathbf{R}L,\mathbf{R}'L'}) = 0}. \tag{2.44}$$

2.3.2 Energy Linearization

The KKR-ASA secular equation (2.44) is related to an energy linearization of the radial amplitude $\varphi_{\mathbf{R}l}(r,E)$ in the neighborhood of some energy $E = E_{\nu,\mathbf{R}l}$.

Taylor-expanding the radial amplitude $\varphi_{Rl}(r,E)$ then takes care of the energy dependence:

$$\boxed{\varphi_{\mathbf{R}l}(r,\,E) = \phi_{\mathbf{R}l}(r) + \dot{\phi}_{\mathbf{R}l}(r)(E - E_{\nu,\,\mathbf{R}l}) + ...} \tag{2.45}$$

with:

$$\phi_{\mathbf{R}l}(r) = \varphi_{\mathbf{R}l}(r, E_{\nu,\mathbf{R}l}) \tag{2.46}$$

$$\dot{\phi}_{\mathbf{R}l}(r) = \dot{\varphi}_{\mathbf{R}l}(r, E_{\nu,\mathbf{R}l}), \tag{2.47}$$

and:

$$\dot{\varphi}_{\mathbf{R}l}(r,\,E) = \frac{d\varphi_{\mathbf{R}l}(r,\,E)}{dE}. \tag{2.48}$$

2.3.3 Linear Muffin Tin Orbitals

LMTOs are constructed from the envelope function $K_L(r_{\mathbf{R}})$ by replacing the radial amplitudes $K_l(r)$ and $J_l(r)$ inside all atomic spheres by linear combinations of the functions $\phi_{\mathbf{R}l}(r)$ and $\dot{\phi}_{\mathbf{R}l}(r)$ by using the Wronskians at $r = s_{\mathbf{R}}$:

$$K_l(r) \rightarrow -\{K,\dot{\phi}\}_{\mathbf{R}l}\phi_{\mathbf{R}l} + \{K,\phi\}_{\mathbf{R}l}\dot{\phi}_{\mathbf{R}l} \tag{2.49}$$

$$J_l(r) \rightarrow -\{J,\dot{\phi}\}_{\mathbf{R}l}\phi_{\mathbf{R}l} + \{J,\phi\}_{\mathbf{R}l}\dot{\phi}_{\mathbf{R}l} \tag{2.50}$$

using the notation: $\{K,\phi\}_{\mathbf{R}l} = -\{K_l(r),\phi_{\mathbf{R}l}(r)\}_r = s_{\mathbf{R}}$

The LMTO $\chi_{\mathbf{R}l}(\mathbf{r})$ is defined as:

$$\chi_{\mathbf{R}l}(\mathbf{r}) = \begin{cases} -\{K,\dot{\phi}\}_{\mathbf{R}l}\phi_{\mathbf{R}l} + \{K,\phi\}_{\mathbf{R}l}\dot{\phi}_{\mathbf{R}l} & (r_R \leq s_R) \\ -\sum_{L'} S_{RL,R'L'} \Big\{ -\{J,\dot{\phi}\}_{\mathbf{R}'l'}\phi_{\mathbf{R}'l'}(r_{\mathbf{R}'}) & \\ \qquad +\{J,\phi\}_{\mathbf{R}'l}\dot{\phi}_{\mathbf{R}'l'}(r_{\mathbf{R}'}) \Big\} & (r'_R \leq s'_R, R' \neq R) \\ K_L(r_R) & (r \in I) \end{cases} \tag{2.51}$$

Using the variational procedure is equivalent to solving the Schrodinger Equation:

$$\langle\psi(\mathbf{r})| -\nabla^2 + V(\mathbf{r})|\psi(\mathbf{r})\rangle = 0. \tag{2.52}$$

If the trial wavefunction $\psi(\mathbf{r})$ is a linear combination of basis function $\chi_i(\mathbf{r})$, the variational procedure leads to the eigenvalue problem:

$$det(EO_{ij} - H_{ij}) = 0. \tag{2.53}$$

In the ASA, the Hamiltonian and the overlap matrices are defined by:

$$H_{ij} = \int_A \chi_i(\mathbf{r})[-\nabla^2 + V(\mathbf{r})]\chi_j(\mathbf{r})d^3(\mathbf{r}) + \int_I \chi_i(\mathbf{r})(-\nabla^2)\chi_j(\mathbf{r})d^3(\mathbf{r}), \tag{2.54}$$

$$O_{ij} = \int_A \chi_i(\mathbf{r})\chi_j(\mathbf{r})d^3(\mathbf{r}). \tag{2.55}$$

At this stage, matrix notation is used and quantities of type $X_{\mathbf{R}L,\mathbf{R}'L'}$ are collected into a matrix X ($X = S, O, H$); while quantities like $\{K,\phi\}$ are diagonal matrices.

Using the LMTO basis (2.51) for the eigenvalue problem in the ASA leads to complicated Hamiltonian and Overlap matrices, which can be significantly simplified by rewritting them in terms of an auxiliary matrix M (whose transpose is M^T):

$$M = \{K,\dot{\phi}\} - \{J,\dot{\phi}\}S. \tag{2.56}$$

The Hamiltonian and Overlap matrices in terms of M then become:

$$O = M^T M \tag{2.57}$$

$$H = M^T E_\nu M - M^T(\{K,\phi\} - \{J,\phi\}S). \tag{2.58}$$

Using M, the original LMTO basis (2.51) can be transformed into an orthogonal basis set that change the original eigenvalue problem (2.53) into:

$$det(E\delta_{\mathbf{R}L,\mathbf{R}'L'} - H^{orth}_{\mathbf{R}L,\mathbf{R}'L'}) = 0. \tag{2.59}$$

the new Hamiltonian corresponding to the orthogonal basis is then:

$$\begin{aligned} H^{orth} &= (M^T)^{-1} H M^{-1} \\ &= E_\nu - (\{K,\phi\} - \{J,\phi\}S)(\{K,\dot{\phi}\} - \{J,\dot{\phi}\}S)^{-1}. \end{aligned} \tag{2.60}$$

Using the Wronskian relation:

$$\{J,\phi\}_{\mathbf{R}l}\{K,\dot{\phi}\}_{\mathbf{R}l} - \{J,\dot{\phi}\}_{\mathbf{R}l}\{K,\dot{\phi}\}_{\mathbf{R}l} = \frac{w}{2} \tag{2.61}$$

(2.60) becomes:

$$\boxed{H^{orth} = E_\nu - \frac{\{K,\phi\}}{\{K,\dot{\phi}\}} + \frac{w}{2}\frac{1}{\{K,\dot{\phi}\}}S\left(1 - \frac{\{J,\dot{\phi}\}}{\{K,\dot{\phi}\}}S\right)^{-1}\frac{1}{\{K,\dot{\phi}\}}}. \tag{2.62}$$

2.3.4 Potential Parameters

The energy-dependent potential function $P_{\mathbf{R}l}(E)$ is defined previously in (2.38):

$$P_{\mathbf{R}l}(E) = \frac{\{K,\varphi(r,\,E)\}_{\mathbf{R}l}}{\{J,\varphi(r,\,E)\}_{\mathbf{R}l}}. \tag{2.63}$$

Using the energy linearization condition above (2.45) for $\varphi_{\mathbf{R}l}(r,E)\}$ and keeping only the first 2 terms of the Taylor expansion allows $P_{\mathbf{R}l}(E)$ to be written as a fraction of 2 linear functions (uniquely determined by 3 parameters $C_{\mathbf{R}l}, \gamma_{\mathbf{R}l}, \Delta_{\mathbf{R}l}$).

$$P_{\mathbf{R}l}(E) = \frac{E - C_{\mathbf{R}l}}{\Delta_{\mathbf{R}l} + \gamma_{\mathbf{R}l}(E - C_{\mathbf{R}l})}. \tag{2.64}$$

This parametrization of $P_{\mathbf{R}l}(E)$ is correct up to second order in $(E - E_{\nu,\mathbf{R}l})$

The potential parameters are defined in terms of the Wronskians:

$$C_{\mathbf{R}l} = E_{\nu,\mathbf{R}l} - \frac{\{K,\varphi(r,\,E)\}_{\mathbf{R}l}}{\{J,\varphi(r,\,E)\}_{\mathbf{R}l}} \tag{2.65}$$

$$\Delta_{\mathbf{R}l} = \frac{w}{2}\frac{1}{\{K,\dot{\phi}\}^2}_{\mathbf{R}l} \tag{2.66}$$

$$\gamma_{\mathbf{R}l} = \frac{\{J,\dot{\phi}\}_{\mathbf{R}l}}{\{K,\dot{\phi}\}_{\mathbf{R}l}} \tag{2.67}$$

From(2.60) and (2.65), the orthogonal Hamiltonian in terms of the potential parameters is:

$$\boxed{H^{orth} = C + \sqrt{\Delta}S(1 - \gamma S)^{-1}\sqrt{\Delta}}, \tag{2.68}$$

where C, Δ, γ are diagonal matrices corresponding to potential parameters $C_{\mathbf{R}l}$ (the center),$\gamma_{\mathbf{R}l}$ (the distortion), and $\Delta_{\mathbf{R}l}$ (the width) of the unhybridized $\mathbf{R}l$ band.

2.3.5 TB-MTOs

Because of the infinite range of the MTOs basis, screening constants $\alpha_{\mathbf{R}l}$ for each band index $\mathbf{R}l$ are introduced so that the tail-cancellation condition (2.43) remained unchanged but the range of the MTOs are shortened:

$$\sum_{\mathbf{R}L} a^{\alpha}_{\mathbf{R}L}[P^{\alpha}_{\mathbf{R}l}(E)\delta_{\mathbf{R}L,\mathbf{R}'L'} - S^{\alpha}_{\mathbf{R}L,\mathbf{R}'L'}] = 0, \tag{2.69}$$

where the screened matrices are related to the unscreened ones by:

$$P^{\alpha}(E) = P(E) + P(E)\alpha P^{\alpha}(E) = P(E)[1 - \alpha P(E)]^{-1} \tag{2.70}$$

$$S^{\alpha}(E) = S(E) + S(E)\alpha S^{\alpha}(E) = (1 - \alpha S(E))^{-1}S(E) \tag{2.71}$$

The set of screening constants $\alpha = \beta_{\mathbf{R}l}$ that yields the shortest range MTOs is called the Tight Binding representation, in which the range of $S^{\beta}_{\mathbf{R}L,\mathbf{R}'L'}$ is limited to first- and second-nearest neighbors.

To obtain energy bands, the TB representation of (2.68) is used, but for transport problem, we are only interested in $P^{\beta}(E)$ at a fixed energy (the Fermi energy E_F). The potential functions is calculated from the potential parameters (2.65) obtained by solving the Kohn-Sham equations above self-consitently.

2.4 Wavefunction Matching

Wavefunction Matching is used to solve the transport problem in 2 steps [5]:

1. The transport problem is solved for the leads, which is an ideal wire.
2. The leads' solutions are matched to that of the scattering regions using the suitable boundary conditions.

Central to the transport problem (in which the system is discretized into cells with index i along the direction of transport) is the Equation of Motion (EOM):

$$(E\mathbf{I} - \mathbf{H_i})\mathbf{\Psi_i} + \mathbf{B}\mathbf{\Psi_{i-1}} + \mathbf{B}^\dagger\mathbf{\Psi_{i+1}} = 0, \tag{2.72}$$

where $\mathbf{\Psi}$ is a column vector of N elements, H_i is the $N \times N$ Hamiltonian matrix of cell i, $\mathbf{B}$ and $\mathbf{B}^\dagger$ are the $N \times N$ coupling matrices between neighboring cells.

2.4.1 Lead Modes

The leads can be considered as ideal wires (whose potential is periodic in the direction of the wire) with 3D translational symmetry, capable of supporting Bloch states. As the potential is the same in each cell, the Hamiltonian is independent of the cell position or index i along $\hat{z}$.

We then have :

$$\mathbf{\Psi_{i+1}} = \lambda\mathbf{\Psi_i}, \tag{2.73}$$

where $\lambda = e^{ik_z a}$, a is the period along the $\hat{z}$-direction.

From (2.72) and (2.73), one has the generalized eigenvalue problem whose dimension is $2N$:

$$\left[\begin{pmatrix} E\mathbf{I} - \mathbf{H} & \mathbf{B} \\ \mathbf{I} & 0 \end{pmatrix} - \lambda \begin{pmatrix} -\mathbf{B}^\dagger & 0 \\ 0 & \mathbf{I} \end{pmatrix}\right] \begin{pmatrix} \mathbf{\Psi}_i \\ \mathbf{\Psi}_{i-1} \end{pmatrix} = 0. \tag{2.74}$$

The physical solutions of (2.74) constitute $\lambda_m(\pm)$ $(m = 1, 2, ..., M)$ where $M << N$, where $(+)$ denotes right-going states (both Bloch and evanescent waves) while $(-)$ denotes left-going states. Corresponding to an eigenvalue $\lambda_m(\pm)$ is a state $\mathbf{u_m}(\pm)$ such that one can construct the following matrix with dimension $N \times M$ (from the first N elements of the $2N$-element eigenvectors of (2.74)):

$$\mathbf{U}(\pm) = (\mathbf{u_1}(\pm)...\mathbf{u_M}(\pm)). \tag{2.75}$$

With cell $i = 0$ as the origin, the right- and left-going modes in this cell $\mathbf{\Psi_0}(\pm)$ can be written as linear combinations of these right- and left-going states $\mathbf{U}(\pm)$:

$$\mathbf{\Psi_0}(\pm) = \mathbf{U}(\pm)\mathbf{a}(\pm) = \sum_{m=1}^{M} \mathbf{u_m}(\pm)a_m(\pm), \tag{2.76}$$

where $\mathbf{a}(\pm)$ are vectors of arbitrary coefficients of dimensions M.

Hence the general solution $\mathbf{\Psi_0}$ can be written as a linear combination of the right- and left-going modes:

$$\mathbf{\Psi_0} = \mathbf{\Psi_0}(+) + \mathbf{\Psi_0}(-). \tag{2.77}$$

Defining the $M \times M$ diagonal eigenvalue matrices by:

$$(\mathbf{\Lambda}(\pm))_{nm} = \delta_{nm}\lambda_{nm}(\pm). \tag{2.78}$$

From the Bloch condition of (2.73), the general solutions in other cells can be written as:

$$\begin{aligned} \mathbf{\Psi_i} &= \mathbf{\Psi_i}(+) + \mathbf{\Psi_i}(-) \\ &= \mathbf{U}(+)\mathbf{\Lambda^i}(+)\mathbf{a}(+) + \mathbf{U}(-)\mathbf{\Lambda^i}(-)\mathbf{a}(-) \end{aligned}$$

Following Ando's formalism, the general solution in cell i should be rewritten in the forms:

$$\boxed{\mathbf{\Psi_{i+1}} = \mathbf{F}(+)\mathbf{\Psi_i}(+) + \mathbf{F}(-)\mathbf{\Psi_i}(-)} \tag{2.79}$$

$$\boxed{\mathbf{\Psi_{i-1}} = \tilde{\mathbf{F}}(+)\mathbf{\Psi_i}(+) + \tilde{\mathbf{F}}(-)\mathbf{\Psi_i}(-)} \tag{2.80}$$

where the $N \times N$ matrices $\mathbf{F}(\pm)$ and $\tilde{\mathbf{F}}(\pm)$ are defined as:

$$\mathbf{F}(\pm)\mathbf{U}(\pm) = \mathbf{U}(\pm)\mathbf{\Lambda}(\pm), \tag{2.81}$$

$$\tilde{\mathbf{F}}(\pm)\mathbf{U}(\pm) = \mathbf{U}(\pm)\mathbf{\Lambda^{-1}}(\pm). \tag{2.82}$$

2.4.2 Scattering Problem

A typical transport problem consists of a scattering section inserted between 2 leads (assumed to be ideal wires). Within the scattering section the potential is not periodic and the Schrodinger equation needs to be solved for each cell i along the wire.

Let the scattering region spans the cells $i = 1, ..., S$ and the left lead span cells $i = -\infty, ..., 0$ and right lead span cells $i = S+1, ..., \infty$. Within the leads, the Hamiltonian $\mathbf{H_i}$ does not depend on position, hence : $\mathbf{H_i}(i < 1) = \mathbf{H_L}$ for left lead and $\mathbf{H_i}(i > S) = \mathbf{H_R}$ for right lead.

2.4.2.1 Coupling of the Scattering Region to the Left Lead

Starting with the EOM at cell $i = 0$:

$$(E\mathbf{I} - \mathbf{H_L})\mathbf{\Psi_0} + \mathbf{B}\mathbf{\Psi_{-1}} + \mathbf{B}^\dagger\mathbf{\Psi_1} = 0 \tag{2.83}$$

Using (2.80) and (2.77) for cell $i = -1$, $\mathbf{\Psi_{-1}}$ is:

$$\begin{aligned} \mathbf{\Psi_{-1}} &= \tilde{\mathbf{F}}_\mathbf{L}(+)\mathbf{\Psi_0}(+) + \tilde{\mathbf{F}}_\mathbf{L}(-)\mathbf{\Psi_0}(-) \\ &= \tilde{\mathbf{F}}_\mathbf{L}(+)\mathbf{\Psi_0}(+) + \tilde{\mathbf{F}}_\mathbf{L}(-)\{\mathbf{\Psi_0} - \mathbf{\Psi_0}(+)\} \\ &= \left\{\tilde{\mathbf{F}}_\mathbf{L}(+) - \tilde{\mathbf{F}}_\mathbf{L}(-)\right\}\mathbf{\Psi_0}(+) + \tilde{\mathbf{F}}_\mathbf{L}(-)\mathbf{\Psi_0} \end{aligned} \tag{2.84}$$

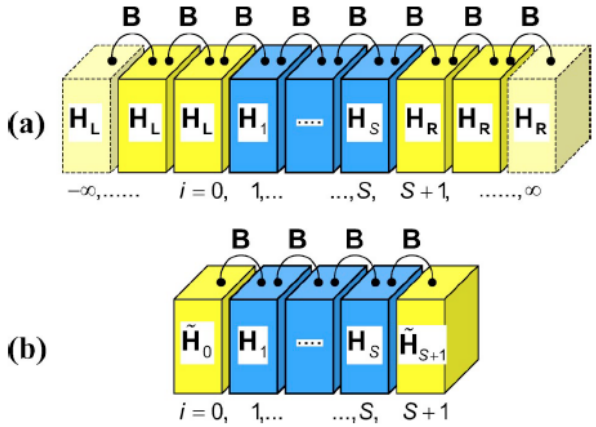

Figure 2.1: Transport Problem discretized into cells (Figure adapted from [5].)

Substituting (2.84) into (2.83) we have:

$$(E\mathbf{I} - \mathbf{H_L})\mathbf{\Psi_0} + \mathbf{B}\left\{[\tilde{\mathbf{F}}_\mathbf{L}(+) - \tilde{\mathbf{F}}_\mathbf{L}(-)]\mathbf{\Psi_0}(+) + \tilde{\mathbf{F}}_\mathbf{L}(-)\mathbf{\Psi_0}\right\} + \mathbf{B}^\dagger\mathbf{\Psi_1} = 0. \tag{2.85}$$

Rearranging gives:

$$\left\{E\mathbf{I} - [\mathbf{H_L} - \mathbf{B}\tilde{\mathbf{F}}_\mathbf{L}(-)]\right\}\mathbf{\Psi_0} + \mathbf{B}^\dagger\mathbf{\Psi_1} = \mathbf{B}[\tilde{\mathbf{F}}_\mathbf{L}(-) - \tilde{\mathbf{F}}_\mathbf{L}(+)]\mathbf{\Psi_0}(+). \tag{2.86}$$

Letting :

$$\tilde{\mathbf{H}}_\mathbf{0} = \mathbf{H_L} - \mathbf{B}\tilde{\mathbf{F}}_\mathbf{L}(-), \tag{2.87}$$

and:

$$\mathbf{Q} = \mathbf{B}[\tilde{\mathbf{F}}_\mathbf{L}(-) - \tilde{\mathbf{F}}_\mathbf{L}(+)], \tag{2.88}$$

Eq. (2.83) becomes:

$$\boxed{(E\mathbf{I} - \tilde{\mathbf{H}}_\mathbf{0})\mathbf{\Psi_0} + \mathbf{B}^\dagger\mathbf{\Psi_1} = \mathbf{Q}\mathbf{\Psi_0}(+)}. \tag{2.89}$$

2.4.2.2 Coupling of the Scattering Region to the Right Lead

Again, starting with the EOM for cell $i = S + 1$:

$$(E\mathbf{I} - \mathbf{H_R})\mathbf{\Psi_{S+1}} + \mathbf{B}\mathbf{\Psi_S} + \mathbf{B}^\dagger\mathbf{\Psi_{S+2}} = 0 \tag{2.90}$$

Using (2.80) $\mathbf{\Psi_{S+2}}$ can be written as:

$$\mathbf{\Psi_{S+2}} = \mathbf{F_R}(+)\mathbf{\Psi_{S+1}}(+), \tag{2.91}$$

since there is no left-going wave in the right lead (only right-going waves)

Substituting (2.91) into (2.90):

$$(E\mathbf{I} - \mathbf{H_R})\mathbf{\Psi_{S+1}} + \mathbf{B}\mathbf{\Psi_S} + \mathbf{B}^\dagger \{\mathbf{F_R}(+)\mathbf{\Psi_{S+1}}(+)\} = 0 \tag{2.92}$$

Rearranging gives:

$$\left\{E\mathbf{I} - [\mathbf{H_R} - \mathbf{B}^\dagger\mathbf{F_R}(+)]\right\}\mathbf{\Psi_{S+1}} + \mathbf{B}\mathbf{\Psi_S} = 0. \tag{2.93}$$

Letting:

$$\tilde{\mathbf{H}}_{\mathbf{S+1}} = \mathbf{H_R} - \mathbf{B}^\dagger\mathbf{F_R}(+), \tag{2.94}$$

Eq.(2.90) becomes:

$$\boxed{\left(E\mathbf{I} - \tilde{\mathbf{H}}_{\mathbf{S+1}}\right)\mathbf{\Psi_{S+1}} + \mathbf{B}\mathbf{\Psi_S} = 0}. \tag{2.95}$$

2.4.2.3 Scattering Region and Matrix

The EOM in the scattering region ($i = 1, ..., S$) is position-dependent:

$$\boxed{(E\mathbf{I} - \mathbf{H_i})\mathbf{\Psi_i} + \mathbf{B}\mathbf{\Psi_{i-1}} + \mathbf{B}^\dagger\mathbf{\Psi_{i+1}} = 0}. \tag{2.96}$$

Combining (2.89), (2.95) and (2.96) gives the complete set of equations to be solved for the transport problem to determine all possible waves.

The scattering reflection and transmission coefficients can be determined from the amplitudes immediately left and right of the scattering region ($\mathbf{\Psi_0}$ and $\mathbf{\Psi_{S+1}}$).

If the incoming wave $\mathbf{\Psi_0}$ consists of one mode $\mathbf{u}_{L,n}$: $\mathbf{\Psi_0} = \mathbf{u}_{L,n}$ then we have the following definitions for the generalized reflection and transmission probability amplitudes $r_{n'n}$ and $t_{n'n}$:

$$\mathbf{\Psi_0}(-) = \sum_{n'=1}^{M_L} \mathbf{u}_{L,n'}(-)r_{n'n}. \tag{2.97}$$

$$\mathbf{\Psi_{S+1}}(+) = \sum_{n'=1}^{M_R} \mathbf{u}_{R,n'}(+)t_{n'n}, \tag{2.98}$$

where M_L and M_R are the number of modes reflected and transmitted, respectively.

The reflection matrix $\mathbf{R}$ has the dimension $M_L \times M_L$ and the transmission matrix $\mathbf{T}$ has the dimension $M_R \times M_L$. Defining a $N \times M_L$ matrix of all possible incoming modes:

$$\mathbf{C_0}(+) = \mathbf{U_L}(+), \tag{2.99}$$

we then have:

$$\mathbf{C_0}(-) = \mathbf{C_0} - \mathbf{C_0}(+) = \mathbf{U_L}(-)\mathbf{R}, \tag{2.100}$$

$$\mathbf{C_{S+1}}(+) = \mathbf{C_{S+1}} = \mathbf{U_R}(+)\mathbf{T}, \tag{2.101}$$

(2.89), (2.95) and (2.96) then become:

$$(E\mathbf{I} - \tilde{\mathbf{H}}_\mathbf{0})\mathbf{C_0} + \mathbf{B}^\dagger\mathbf{C_1} = \mathbf{Q}\mathbf{U_L}(+) \tag{2.102}$$

$$(E\mathbf{I} - \mathbf{H_i})\mathbf{C_i} + \mathbf{B}\mathbf{C_{i-1}} + \mathbf{B}^\dagger\mathbf{C_{i+1}} = 0 \tag{2.103}$$

$$\left(E\mathbf{I} - \tilde{\mathbf{H}}_{\mathbf{S+1}}\right)\mathbf{C_{S+1}} + \mathbf{B}\mathbf{C_S} = 0 \tag{2.104}$$

Combining (2.102), (2.103) and (2.104) gives the following $N \times (S+2)$ matrix equation:

$$\boxed{(E\mathbf{I} - \mathbf{H}')\mathbf{\Psi} = \mathbf{Q}'} \tag{2.105}$$

$$\mathbf{H}' = \begin{pmatrix} \tilde{\mathbf{H}}_\mathbf{0} & \mathbf{B}^\dagger & \cdots & 0 & 0 & 0 \\ \mathbf{B} & \ddots & \mathbf{B}^\dagger & 0 & 0 & 0 \\ 0 & \mathbf{B} & \mathbf{H}_i & \mathbf{B}^\dagger & \cdots & 0 \\ \vdots & \vdots & \ddots & \ddots & \ddots & \vdots \\ 0 & 0 & 0 & \ddots & \ddots & \mathbf{B}^\dagger \\ 0 & 0 & 0 & \cdots & \mathbf{B} & \tilde{\mathbf{H}}_{\mathbf{S+1}} \end{pmatrix} \tag{2.106}$$

$$\mathbf{\Psi} = \begin{pmatrix} \mathbf{C}_0 \\ \vdots \\ \mathbf{C}_i \\ \vdots \\ \mathbf{C}_{S+1} \end{pmatrix}; \mathbf{Q}' = \begin{pmatrix} \mathbf{B}\left[\tilde{\mathbf{F}}_L(-) - \tilde{\mathbf{F}}_L(+)\right]\mathbf{U}_L(+) \\ \vdots \\ 0 \\ \vdots \\ 0 \end{pmatrix} \tag{2.107}$$

Solving (2.106) for $\mathbf{C}_i$ gives all possible waves and the generalized reflection $\mathbf{R}$ and transmission $\mathbf{T}$ matrices.

To calculate the total transmission, transmission matrix elements describing propagating modes have to be selected and those describing evanescent states have to be discarded (Propagating modes have $|\lambda| = 1$). The total transmission is then given by:

$$T(E) = \sum_{n=1,n'=1}^{m_L,m_R} \frac{v_{R,n'}}{v_{L,n}} |t_{n'n}|^2. \tag{2.108}$$

The velocities are given by the expression:

$$v_n = -\frac{2a_z}{\hbar} Im(\lambda_n \mathbf{u}^\dagger{}_n \mathbf{B}^\dagger \mathbf{u}_n). \tag{2.109}$$

where a_z is the periodic in the z direction.(the sign is used to distinguish right from left-going modes)

2.4.3 Wavefunction Matching in TB-MTOs Basis

The formalism is exactly the same as presented in the previous section, just the basis is changed. Also, because of the 2D translational symmetry in the principal layers I, states can be characterized by a lateral wave vector $k_{||}$. The tail-cancellation condition (2.69) is equivalent to (2.105) :

$$\mathbf{P} - \tilde{\mathbf{S}} = (E\mathbf{I} - \mathbf{H}'). \tag{2.110}$$

Thus the EOM in transport problem using TB-MTO basis is:

$$-S^{\mathbf{k}_{||}}_{I,I-1}\mathbf{C}_{I,I-1} + \left(P_{I,I}(E) - S^{\mathbf{k}_{||}}_{I,I}\right) - S^{\mathbf{k}_{||}}_{I,I+1}\mathbf{C}_{I,I+1} = 0, \tag{2.111}$$

with:

$$S^{\mathbf{k}_{||}}_{I,J} = \sum_{\mathbf{T}\in\{\mathbf{T}_{I,J}\}} S^{\beta}(\mathbf{T})e^{i\mathbf{k}_{||}\cdot\mathbf{T}}, \tag{2.112}$$

where $\{\mathbf{T}_{I,J}\}$ is the set of vectors connecting one lattice site in the I^{th} layer with those in the J^{th} layer.

The final matrix equation to solve to obtain all possible propagating states is (similar to (2.106)):

$$\begin{pmatrix} \left(P-\tilde{S}\right)_{0,0} & -S_{0,1} & 0 & \dots & 0 & 0 \\ -S_{1,0} & (P-S)_{1,1} & -S_{1,2} & \dots & 0 & 0 \\ 0 & -S_{2,1} & (P-S)_{2,2} & \dots & \vdots & 0 \\ \vdots & \vdots & \dots & \ddots & \vdots & 0 \\ 0 & 0 & \dots & \dots & (P-S)_{N,N} & -S_{N,N+1} \\ 0 & 0 & 0 & \dots & -S_{N+1,N} & \left(P-\tilde{S}\right)_{N+1,N+1} \end{pmatrix}$$

$$\times \begin{pmatrix} \mathbf{C}_0 \\ \mathbf{C}_1 \\ \mathbf{C}_2 \\ \vdots \\ \mathbf{C}_N \\ \mathbf{C}_{N+1} \end{pmatrix} \equiv \begin{pmatrix} S_{0,-1}\left[F^{-1}_{\mathcal{L}}(+) - F^{-1}_{\mathcal{L}}(-)\right]\mathbf{C}_0(+) \\ 0 \\ 0 \\ \vdots \\ 0 \\ 0 \end{pmatrix}$$

where:

$$\tilde{S}_{0,0} = S_{0,0} + S_{0,-1}F^{-1}_{\mathcal{L}}(-) \tag{2.113}$$

$$\tilde{S}_{N+1,N+1} = S_{N+1,N+1} + S_{N+1,N+2}F_{\mathcal{R}}(+) \tag{2.114}$$

The Green function $\mathbf{g}$ is defined as: $\mathbf{g} = \mathbf{P} - \tilde{\mathbf{S}}$ so that the transmission and reflection matrix elements between Bloch states ν and μ are:

$$t_{\mu\nu} = \left(\frac{v_\mu}{v_\nu}\right)^{1/2} \left\{U_{\mathcal{R}}^{-1}(+)\, g_{N+1,0} S_{0,-1} \left[F_{\mathcal{L}}^{-1}(+) - F_{\mathcal{L}}^{-1}(-)\right] U_{\mathcal{L}}(+)\right\}_{\mu\nu}, \tag{2.115}$$

$$r_{\mu\nu} = \left(\frac{v_\mu}{v_\nu}\right)^{1/2} \left\{U_{\mathcal{L}}^{-1}(-) \left\langle g_{0,0} S_{0,-1} \left[F_{\mathcal{L}}^{-1}(+) - F_{\mathcal{L}}^{-1}(-)\right] - 1\right\rangle U_{\mathcal{L}}(+)\right\}_{\mu\nu} \tag{2.116}$$

where v_μ and v_ν are the corresponding group velocities in each mode, and is given by:

$$v_\mu(\pm) = \frac{id}{\hbar}\left[\mathbf{u}_\mu^\dagger(\pm)\, S_{I,I+1}^{\mathbf{k}_\parallel} \mathbf{u}_\mu(\pm)\, \lambda_\mu - H.c.\right]. \tag{2.117}$$

Finally, the conductance per spin channel is:

$$\boxed{G^\sigma = \frac{e^2}{h} \sum_{\mu,\nu,\mathbf{k}_{||}} Tr\{T^\sigma_{\mu,\nu}(\mathbf{k}_{||})\} = \frac{e^2}{h} \sum_{\mu,\nu,\mathbf{k}_{||}} Tr\{t_{\mu,\nu}(\mathbf{k}_{||}) t^\dagger_{\mu,\nu}(\mathbf{k}_{||})\}}. \tag{2.118}$$

2.5 Spin Orbit Coupling and Relativistic Corrections

To fully take into account electron spin, the Dirac Equation with a four-component wavefunction should be used. However, in actual calculations, the energy bands of spin up and spin down channel are calculated using a two-component scalar relativistic Hamiltonian:

$$\mathcal{H}^{\mathbf{SR}} \mathbf{\Psi}(\mathbf{r}) = \varepsilon \mathbf{\Psi}(\mathbf{r}). \tag{2.119}$$

The scalar relativistic Hamiltonian has a rather simple form inside an atomic sphere in the Atomic-Sphere-Approximation [6]:

$$\mathcal{H}^{SR}_{\alpha\beta} = \left[-\nabla^2 + v(r) - \frac{1}{c^2}\left[(\varepsilon - v(r))^2 + \frac{\partial v(r)}{\partial r}\frac{\partial}{\partial r}\right]\right]\delta_{\alpha\beta} + \left[\frac{\delta E_{xc}}{\delta \rho_{\alpha\beta}(\mathbf{r})} - \frac{\delta E_{xc}}{\delta \rho(\mathbf{r})}\delta_{\alpha\beta}\right], \tag{2.120}$$

where $v(r)$ is the relativistic form of the Kohn-Sham effective potential described in the previous section, α and β are the spin indices. The electronic density $\rho(\mathbf{r})$ is the trace of the density matrix $\boldsymbol{\rho}(\mathbf{r})$ whose matrix element is $\rho_{\alpha\beta}(\mathbf{r})$:

$$\rho_{\alpha\beta}(\mathbf{r}) = \sum_{i,\mathbf{k}}^{\varepsilon_F} [\mathbf{\Psi}(\mathbf{r})^{i,\mathbf{k}}_\beta(\mathbf{r})]^* \mathbf{\Psi}(\mathbf{r})^{i,\mathbf{k}}_\alpha(\mathbf{r}). \tag{2.121}$$

Spin Orbit Coupling is taken into account by adding a term $\mathcal{H}^{\mathbf{SO}}$ to (2.119), forming the Pauli Hamiltonian :

$$(\mathcal{H}^{\mathbf{SR}} + \mathcal{H}^{\mathbf{SO}})\mathbf{\Psi}(\mathbf{r}) = \varepsilon \mathbf{\Psi}(\mathbf{r}). \tag{2.122}$$

Since we are dealing with spherically symmetric potential, the spin-orbit coupling term has the form:

$$\mathcal{H}^{\mathbf{SO}} = \frac{1}{2}\xi(r)\mathbf{l}.\sigma = c^{-2}\frac{1}{2}\frac{\partial v(r)}{\partial r}.\begin{pmatrix} l_z & l_- \\ l_+ & -l_z \end{pmatrix} \tag{2.123}$$

With spin-orbit coupling effect included, the two spin bands are coupled, and in the end there no longer be two clearly separated channels. The calculation is performed self-consistently for $\mathcal{H}^{\mathbf{SR}}$ to obtain all the potentials, then in the transport code, the Pauli Hamiltonian is used, taking into account SOC ($\mathcal{H}^{\mathbf{SO}}$).

Chapter 3

Review of Experimental Methods and 2CSR Model

3.1 A brief introduction of the Two-Current Series Resistor Model

The Two-Current Series Resistor (2CSR) model, introduced by MSU group [7], [2] to analyze their CPP-GMR data, offers a straightforward way to extract all the relevant spin-dependent transport parameters like resistivity, resistance, and anisotropy scattering parameters associated with the bulk and the interface of the multilayers in CPP structure in the limit where the layer thicknesses are much smaller than their corresponding spin diffusion lengths. The model takes into account the contributions from two separate spin channels (↑) and (↓) as two independent current-carrying channel connected in parallel (no spin-flipping is allowed). The structure used in the experiment consists of N bilayers of alternating ferromagnetic (F) and non-magnetic (N) materials (each with its own resistivity ρ_{F} and ρ_{N} respectively). The total resistance of such a model is calculated to be the equivalent resistance of two parallelly-connected channels:

$$R_T = \frac{R_1 \cdot R_2}{R_1 + R_2}. \tag{3.1}$$

More specifically, the total resistance (for each spin channel) is decomposed into bulk ($\rho_i t_i$, with i = F, N, and t_i being the thickness of the F or N layer) and interface ($R_{\mathrm{F/N}}$) components. Associated with each resistive component is an asymmetry coefficient arising due to the spin-polarized currents: β for bulk resistivity and γ for interface resistance - together with these

parameters, the effective resistivity ρ_{F}^{*} and effective interface resistance $R_{\mathrm{F/N}}^{*}$ are defined to be:

$$\rho_F^* = \frac{\rho_F}{1 - \beta^2}, \tag{3.2}$$

$$R_{F/N}^* = \frac{R_{F/N}}{1 - \gamma^2}. \tag{3.3}$$

With all the parameters defined as above, the 2CSR model equations read:

$$AR_T(AP) = 2AR_{S/F}^* + N(\rho_F^* t_F + \rho_N t_N + 2AR_{F/N}^*), \tag{3.4}$$

for the case of anti-parallel (AP) alignment of magnetizations in adjacent F layers ($AR_{\mathrm{S/F}}$ is the interface resistance between the superconducting leads and F layer)

$$AR_T(P) = AR_T(AP) - \frac{N^2(\beta\rho_F^* t_F + 2\gamma AR_{F/N}^*)^2}{AR_T(AP)}, \tag{3.5}$$

for the case of parallel (P) alignment of magnetizations in adjacent F layers.

Equation (3.5) can be rewritten as:

$$A\sqrt{R_T(AP)[R_T(AP) - R_T(P)]} = N[\beta\rho_F^* t_F + 2\gamma AR_{F/N}^*], \tag{3.6}$$

$$A\sqrt{R_T(AP)[R_T(AP) - R_T(P)]} = \frac{\beta\rho_F^* t_T}{2} + N[2\gamma AR_{F/N}^*]. \tag{3.7}$$

Eq.(3.6) applies to samples with fixed t_{F} ($t_{\mathrm{F}} \neq t_{\mathrm{N}}$), while (3.7) applies to those with $t_{\mathrm{F}} = t_{\mathrm{N}}$. t_T is the total thickness of the sample, i.e. $t_T = N(t_{\mathrm{F}} + t_{\mathrm{N}})$.

3.2 Experimental details

3.2.1 Experimental Preparation and Characterization of Samples

3.2.1.1 Overview

Typical multilayer samples used for CPP GMR measurements in [1] is shown in Fig. 3.1. The samples used consist of alternating layers of ferromagnetic (F) and non-magnetic (N) materials, Co and Ag respectively. These two constituent metals are used because Co and Ag are immiscible, ensuring minimal intermixing at the interfaces in the multilayers.

The samples are prepared by means of dc sputtering. To ensure consistent quality across all the samples, sputtering conditions like chamber gas pressure and temperature, sputtering voltage and current are held constant. The layered structure are sputtered onto 0.5" square c-axis orientated single crystal sapphire. Measurement results with test samples based on silicon substrates are similar, thus eliminating the dependence on substrate material.

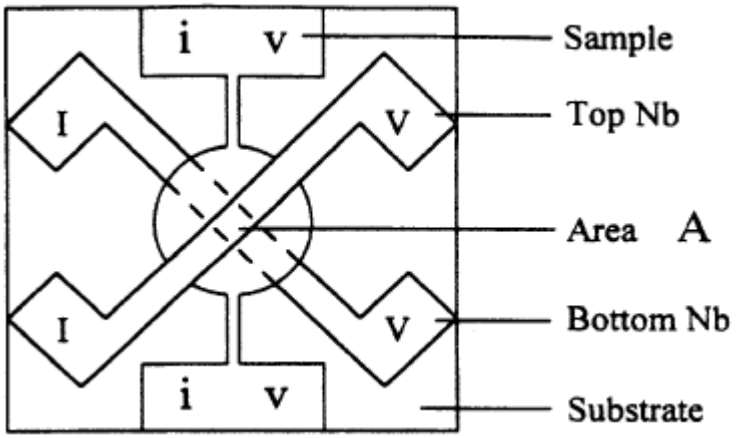

Figure 3.1: Shape of sample. The sample consists of alternating layers of Co and Ag. These are sandwiched between two Nb strips which serve as leads for CPP measurements (figure adapted from [1]).

Each sample consists of alternating layers of Co and Ag sandwiched between two Nb strips (Fig. 3.1) which serve as leads for CPP measurement. The non-overlapping projections from each layers are produced by means of a mask that is introduced during the sputtering of each layers. The total thickness t_T of the sample are fixed at 720 nm to be consistent with an integer number of bilayers. Sample with different thicknesses for the Co and Ag layers are fabricated for the measurements.

The distribution of bilayer thicknesses of the samples was verified by means of a $\theta - 2\theta$ x-ray diffraction, whose results showed that the bilayer thickness is 4% less than intended. A Dektac sample profilometer verified the total thickness to be less than 5 % of the intended 720 nm. Cross-sectional TEM measurements of the samples showed that after a few uniform layers, columnar growth with width ∼20-40 nm begins, resulting in sharp but incoherent interfaces. More details on characterizations' results are presented in the next section.

The measurement of the CPP resistance R_T is conducted by passing a current $I = 50\,mA$ into one Nb strip and extracting it from the other using a bridge circuit [8] with a superconducting quantum interference device (SQUID) null detector to balance the voltage difference V between the strips against that produced by a balancing current I_b with a reference resistor $(1.84 \pm 0.02\,\mu\Omega)$ R_r. The measured ratio, $c = I_b/I$, then gives $R_T = (I_b/I)R_r$. The largest uncertainty in R_T is the 1 % uncertainty in the reference resistor. Except occasional samples

with a particularly small $R_T < 10^{-8}\,\Omega$, the uncertainty in AR_T is dominated by the area. Surface profiler places this uncertainty at about 2-5 %.

The total resistance of the CPP multilayers was experimentally measured as a function of the applied magnetic field H at 4.2K for different samples in which the total thickness of the multilayer is fixed while t_F is kept constant (t_N is varied) or while $t_F = t_N$ (either both are constant or varied). The AP state was either achieved at H_0 (no magnetic field applied) or H_{pk} (peak magnetic field measured when the applied H field is reversed), since H_0 is not reproducible under multiple field sweeps; while the P state was achieved at H_s (the saturation field) (Fig. 3.2). It was observed that the resistance $AR(AP)$ is better approximated by $AR(H_0)$ than $AR(H_{pk})$. $AR(P)$ is the resistance measured at $H = H_s$.

3.2.1.2 Details of Characterization of Samples

Little information has been found about the characterization of Co/Cu samples from MSU group - most of the information found is X-Ray Diffraction (XRD), Transmission Electron Microscopy (TEM) and Nuclear Magnetic Resonance (NMR) studies of Co/Ag samples from S.F.Lee PhD thesis (MSU, 1994) [10], and the results of those characterizations will be summarized in this section. It was learned from these characterizations that the samples have polycrystalline structures (Ag has fcc(111) and Co has either fcc(111) or hcp(0001)).

The large-angle X-Ray 2θ scan (Fig.3.3) with the x-ray wavelength $\lambda = 1.54A^\circ$ was used to study the distribution of bilayer thicknesses of the samples. They shows a series of distinct peaks, corresponding to the constructive interferences from bulk Ag and Nb (at roughly 38°), from bulk Co (44°), and from the multilayer periodicity (the satellite peaks in between the bulk peaks). These satellite peaks' positions allow calculations of the bilayer thickness using the Bragg's Law for diffraction.

All the bilayer thicknesses derived from XRD studies were within 4% of the intended value (either by SUPREX fit or by linear fit of n versus $2sin\theta/\lambda$). Besides, it was mentionned in Lee's thesis that rocking curves scan show peaks with full width at half maximum (FWHM) of 12°, indicating a distribution of crystal orientations in the samples (with the majority lying within ±6° of the preferred direction).

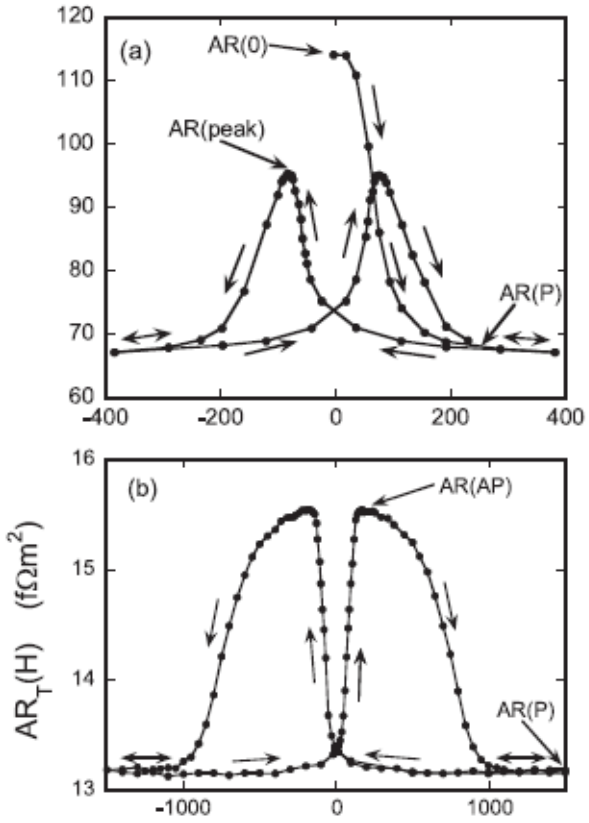

Figure 3.2: (a) $CPP - AR_T(H)$ of a [Co(6nm)/Ag(6nm)]$_6$ sample at 4.2K. The resistance $AR(0)$ corresponds to a field H_0 (in the as-prepared sample), $AR(P)$ corresponds to the saturation field H_s, and AR(peak) corresponds to a field of local maximum after saturation is H_{Pk}. $AR(0)$ is not reproducible after multiple field sweeps. (b) $CPP - AR_T(H)$ of a [Co(8nm)/Cu(10nm)/Co(1nm)/Cu(10nm)]$_4$ multilayer. Stable $AR(AP)$ reproducible after multiple field sweeps. [9].

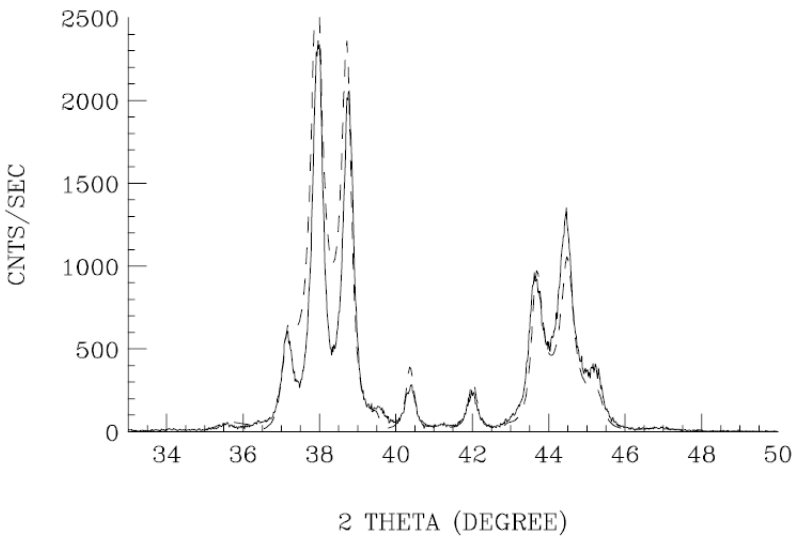

Figure 3.3: Intensity (Counts/Second) vs 2θ of Co/Ag sample with $t_{\mathrm{Co}} = t_{\mathrm{Ag}} = 6nm$. The dashed line is a fit from with SUPREX (a computer program to fit x-ray spectra of multilayered samples). Figure adapted from [10]

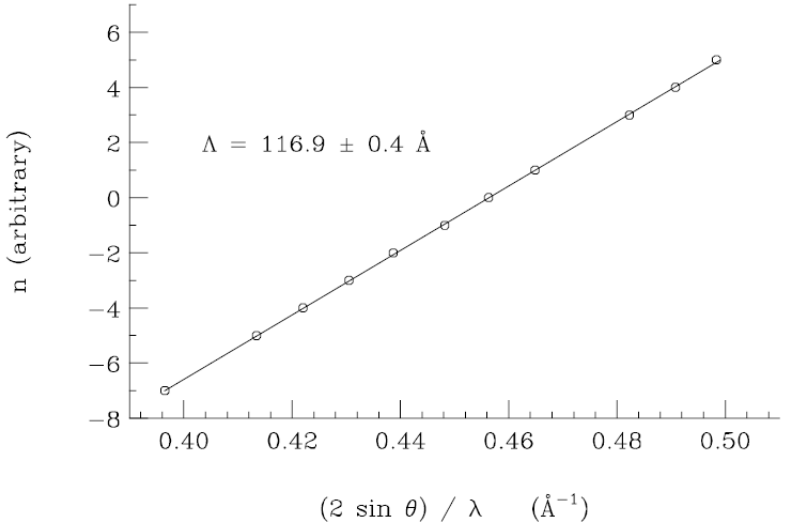

Figure 3.4: The slope of the linear fit gives Λ, the bilayer thickness (using Bragg's Law). Figure adapted from [10]

TEM structural analysis (from sliced samples) showed columnar growth present in the multilayer after a few initial monolayers, the schematic of which is in Fig. 3.5. NMR studies show that Co layers in Co/Ag samples are mixtures of fcc Co, hcp Co and stacking faults. Large amount of strains were found in both Co and Ag layers (due to the large lattice mismatch between them).

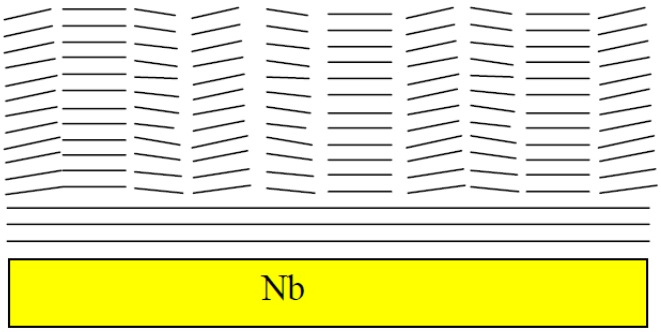

Figure 3.5: Schematic of the Co/Ag sample studied by TEM showing columnar growth after a few intial layers. Figure adapted from [10]

Although information about Co/Cu sample characterizations are not available by MSU group, there were published results by other groups (most notably by S.Pizzini *et al.*). In [11] S.Pizzini *et al.* presented X-ray Diffraction, X-ray Reflectivity and X-ray Absorption Spectroscopy (XAS) studies of Co/Cu samples grown by thermal evaporation in ultrahigh vacuum. Despite the fact that Co and Cu have very similar lattice constants, it was found that in the plane of the layers, the Co lattice expanded while Cu lattice contracts slightly to accomodate the lattice mismatch. (The lattice strain is negligible in the growth direction). Since XRD cannot provide local structural information and can only give some information on the average strain in the direction perpendicular to the interfaces (without being able to distinguish between the strains of Co and Cu layers), XAS and Extended X-ray Absorption Fine Structure (EXAFS) studies provide details of the individual strains in-plane and out-of-plane Cu and Co layers. These studies show that Cu layers appear to be much more ordered than Co layers, specifically, the structural disorder within the Cu layers is comparable to that of bulk Cu, while the disorder within Co layers is much larger than that in bulk Co. Also, consistent with MSU group's characterizations, Co layers have a large concentration of stacking faults, leading to the formation of the more stable hcp domains on top of the fcc ones.

3.2.2 Description of samples

Depending on specific experiments, several sets of samples (Co/Ag, Co/AgSn, Co/Cu) were used in order to extract relevant parameters. Linear behaviors of $AR(AP)$ and $\{(AR(AP) - AR(P)) \times AR(AP)\}^{1/2}$ with respect to N are predicted in the 2CSR model, hence it is important to vary the number of bilayers N. The sample sets are classified into [1, 2]:

1. Fixed total thickness t_T, fixed t_F: the number of bilayers N is varied by varying t_N.
2. Fixed total thickness t_T, fixed t_N: the number of bilayers N is varied by varying t_F.
3. Fixed total thickness t_T, variable $t_F = t_N$: the number of bilayers N is varied by varying $t_F = t_N$.
4. Fixed $t_F = t_N$, the number of bilayers N is varied by varying t_T.

3.3 Extraction of Parameters From CPP-GMR Experimental Data Using The 2CSR

According to the 2CSR model, 6 parameters are to be determined: $AR_{\mathrm{S/F}}$, ρ_F^*, ρ_N, $AR_{\mathrm{F/N}}^*$, β, and γ. In [2], the authors stated that using independently measured value for $AR_{\mathrm{S/F}}$, applying equation (3.4) to samples with fixed t_F or with $t_F = t_N$ yielded ρ_F^*, ρ_N, $AR_{\mathrm{F/N}}^*$. β and γ were extracted from the linear fits of equation (3.6) to samples with fixed t_F and from equation (3.7) with $t_F = t_N$. Thus, using the raw data for $AR(AP)$ and combined $(AR(AP) - AR(P))$, all the 5 parameters were extracted.

Specifically, the extraction of parameters can be understood by explicitly applying (3.4) and (3.5) to the following various series of samples [1].

A. Fixed $t_T = 720\,nm$, fixed $t_{Co} = 6\,nm$, variable t_{Ag} and N:

$$AR(AP) = (2AR_{S/F} + \rho_N t_T) + N[6(\rho_F^* - \rho_N) + 2AR_{F/N}^*], \tag{3.8}$$

$$A[R_T(AP)(R_T(AP) - R_T(P))]^{1/2} = N[6\beta\rho_F^* + 2\gamma AR_{F/N}^*] \tag{3.9}$$

B. Fixed $t_T = 720\,nm$, fixed $t_{Co} = 2\,nm$, variable t_{Ag} and N:

$$AR(AP) = (2AR_{S/F} + \rho_N t_T) + N[2(\rho_F^* - \rho_N) + 2AR_{F/N}^*], \tag{3.10}$$

$$A[R_T(AP)(R_T(AP) - R_T(P))]^{1/2} = N[2\beta\rho_F^* + 2\gamma AR_{F/N}^*]. \tag{3.11}$$

C. Fixed $t_{Co} = t_{Ag} = 6\,nm$, variable t_T and N:

$$AR(AP) = 2AR_{S/F} + N[6(\rho_F^* + \rho_N) + 2AR_{F/N}^*], \tag{3.12}$$

$$A[R_T(AP)(R_T(AP) - R_T(P))]^{1/2} = \frac{1}{2}\beta\rho_F^* t_T + 2N\gamma AR_{F/N}^*. \tag{3.13}$$

D. Fixed $t_T = 720\,nm$, variable $t_{Co} = t_{Ag}$ and N:

$$AR(AP) = (2AR_{S/F} + [\rho_F^* + \rho_N)t_T] + 2AR_{F/N}^*, \tag{3.14}$$

$$A[R_T(AP)(R_T(AP) - R_T(P))]^{1/2} = 360\beta\rho_F^* + 2N\gamma AR_{F/N}^*. \tag{3.15}$$

Linear least-square fits of $AR(AP)$ in (3.8), (3.10), (3.12), and (3.14) give an intercept and a slope which constitue 4 linear equations of $AR_{\mathrm{S/F}}$, ρ_{N}, ρ_{F}^*, and $AR_{\mathrm{F/N}}^*$ that can be simply solved to extract those parameters.In order to extract β and γ, (3.9), (3.11), (3.13) and (3.15) were used in the same way. The result of such an extraction by the MSU group is shown in this table below:

	ρ_{N} (nΩm)	ρ_{Co}^* (nΩm)	$AR_{\mathrm{Co/N}}^*$ (fΩm^2)	β	γ
Co/Ag	10 (3)	107 (10)	0.56 (0.03)	0.48 (0.05)	0.85 (0.03)
Co/AgSn	185 (10)	70	0.67 (0.06)	0.41 (0.12)	0.83 (0.06)
Co/Cu	7 (2)	86 (4)	0.50 (0.02)	0.50 (0.10)	0.76 (0.05)

Figure 3.6: Extracted parameters from the 2CSR Model for Co/Ag, Co/AgSn and Co/Cu multilayers. Figure adapted from [2]

Moreover, according to the authors [12], linear fits of (3.4) to the raw data can also be achieved with independently measured values for $AR_{\mathrm{S/F}}$, ρ_{F} and ρ_{N} on sputtered thin films. It was also claimed by the authors that these independently measured values agreed within mutual uncertainties to those extracted using the 2CSR model [1].

3.4 Limitations of The 2CSR Model

Several doubts have been raised regarding the validity of the assumptions made in the 2CSR Model, most notably are the following [12]:

1. Are the constituent resistances (bulk and interface components) simply additive (in series)?
2. Why are ρ^*_{Co} and β_{Co} extracted from different samples (Co/Ag) and (Co/Cu) using the 2CSR Model different (for samples in the same laboratory)?
3. Are β and γ independent of t_F, t_N, and t_T?
4. Can ρ_N and ρ_F be replaced by their independently measured values?

The largest deviation of CPP-MR from the predictions of the 2CSR Model came from [13], in which the MR(H) of the interleaved $[\mathrm{Co(6nm)Cu(20nm)Co(1nm)Cu(20nm)}]_{\mathrm{N}}$ and separated $[\mathrm{Co(6nm)Cu(20nm)}]_{\mathrm{N}}[\mathrm{Co(1nm)Cu(20nm)}]_{\mathrm{N}}$ samples (with the same magnetization) differed significantly (Fig. 3.7). Co was the chosen F materials because of its known long spin diffusion length ($\approx$ 60nm [13]). Since the total t_F and t_N in each sample are the same (independent of the ordering of the layers), they should have the same MR(H) according to the 2CSR model; however this was clearly not the case.

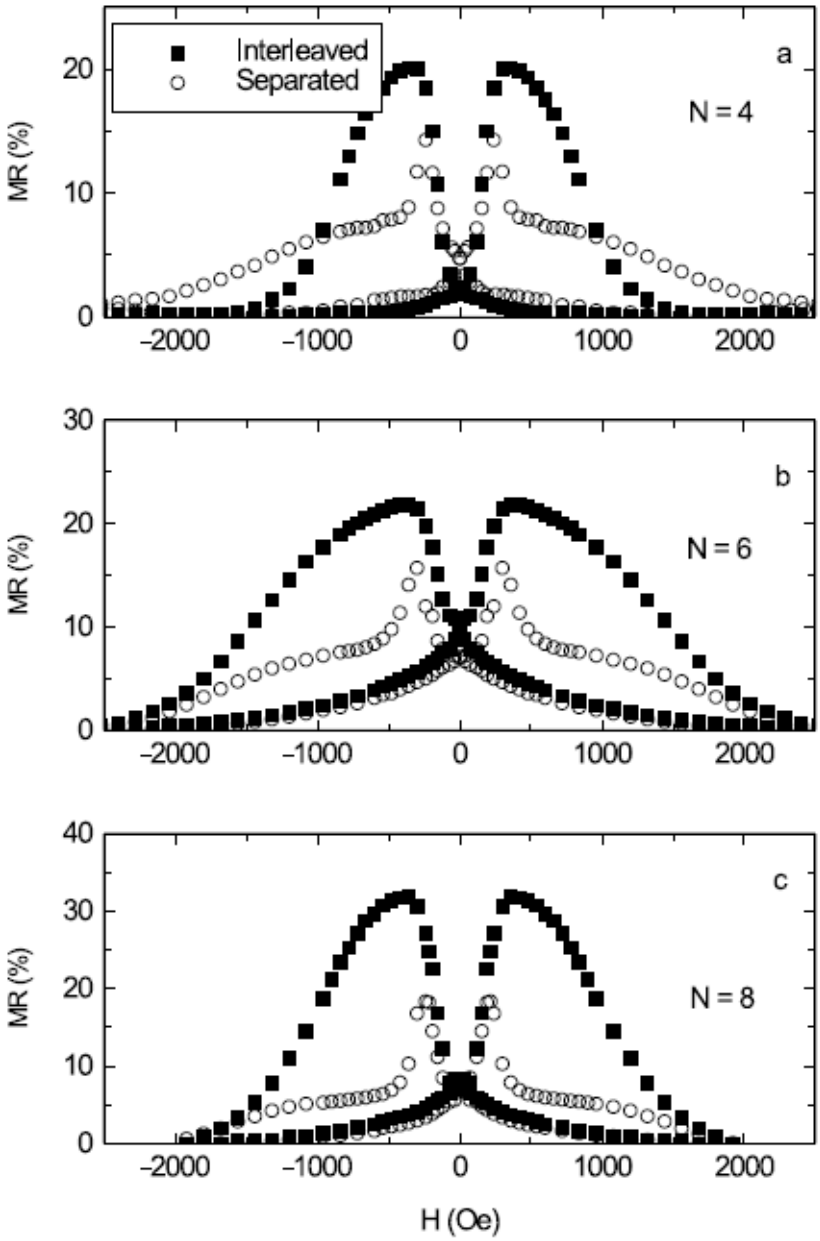

Figure 3.7: MR(H) for interleaved (squares) and separated (circles) Co/Cu multilayers samples with different number of repeats N (indicated in each figure). The MR(H) of the interleaved samples shows a large, single peak, symmetric about $H = 0$, while separated samples show smaller, more complicated structures is much larger than that of the separated ones. Figure adapted from [14].

The authors of [13] attributed the breakdown of the 2CSR Model in this case to the 'mean free path' (MFP) effects, i.e. long electron mean-free path rather than the finite spin diffusion lengths of Co and Cu, and hence argued that the MFP λ_{F} and λ_{N} of each materials are important length scales in CPP-GMR. This was later ruled out by K.Eid *et al.* [15], arguing experimentally that MFP is not a significant length in CPP-GMR, and attributing the observed differences in MR(H) of the separated and interleaved samples to the spin-flip scattering within the F- or N-layer and at the interface between F/N layers. The experimental proof was that the replacement of Cu with a dilute CuGe (2% Ge) alloy (whose alloying is meant to reduce the MFP of Cu) provided no qualitative difference in the MR(H) curves of the interleaved and separated samples employing either Cu or CuGe. They then stated that although the 2CSR Equations are the same for both interleaved and separated samples, the Valet-Fert Equations for them differ in the presence of spin-flip scattering (and must be solved numerically due to their complication). Specifically while t_F and t_N are the only important lengths in the 2CSR Model, t_F/l^F_{sf} and t_N/l^N_{sf} enter as arguments in the exponential terms in VF equations. Subsequently, Eid *et al* [15] attributed the difference of MR(H) for the interleaved and separated samples to spin flipping in the individual F- and N-layer, and at the F/N interfaces. The new parameter δ characterizing spin-flip scattering will be discussed in more details in the next section.

3.5 A New Parameter: Spin-Memory Loss δ

In a multilayer structure of interest, defining a fictitious interfacial layer I between a F- and a N-layer or between two nonmagnetic N_1 and N_2 layer (for every single interface in the multilayer), with t_I and l^I_{sf} being the thickness and spin diffusion length of this layer, δ - the spin-relaxation parameter at that interface, is then defined as:

$$\delta = \frac{t_I}{l^I_{sf}} \tag{3.16}$$

Taking the case of an F/N interface, the fictitious interfacial layer I is further characterized with a resistivity ρ_I (fulfilling the condition $\rho_I t_I = AR^*_{\mathrm{F/N}}$, and 'bulk' scattering anisotropy parameter β_I ($\beta_I = \gamma_{\mathrm{F/N}}$).

Applying Valet-Fert theory [16] to the multilayered system with these fictitious interfacial layers requires the matching of electrochemical potentials and current densities at the boundaries of this I layer with the F- and N-layer. Such a matching depends on t_I/l^I_{sf} or δ_I, and the quantity $\rho_I l^I_{sf}$. Due to the constraint $\rho_I t_I = AR^*_{\mathrm{F/N}}$, we have $\rho_I l^I_{sf} = AR^*_{\mathrm{F/N}}/\delta_I$. The maching

is then entirely controlled by the parameter δ_I, allowing its values to be extracted from the VF solutions. (The exact same principles apply to the case of two nonmagnetic metals N_1 and N_2 instead of F and N).

The value of δ extracted from the above principle for Co|Cu interface is 0.25 [15]. Although it was argued that even with the inclusion of a small δ (≈ 0.25), the use of the 2CSR and VF theory to extract parameters in previously published work is still justified, as δ does not seem to significantly affect AR(AP) or AΔR of interleaved or simple $[F/N]_N$ multilayered samples, the authors of [15] also acknowledged the fact that "if spin-flipping at the interface is eventually confirmed, some parameters (from the original 2CSR model) may need to be slightly modified"

Chapter 4

CPP GMR of Co|Cu

4.1 Computational details and numerical tests

4.1.1 Input Geometries and Generated Potentials

All calculated structures consist of two leads (pure Cu) with a scattering region sandwiched in between. The scattering region could be a finite section of bulk Cu with Co impurites (of varying concentration) or vice versa (a bulk section of Co with Cu impurities of varying concentration); or a multilayered structure of alternating Co and Cu layers. The latter structure is called current-perpendicular-to-plane (CPP) geometry and is used to study GMR effect.

In the transport problem, there is a certain direction (z axis) of current flowing while the x-y plane has in-plane translational symmetry. To model substitutional alloy disorder, we take 5×5 lateral supercell in x-y plane, which is repeated indefinitely. Within one supercell, the on-site potentials are randomly distributed according to the concentration. The length of the scattering region can be extended by repeating a chosen layer a certain number of times using a code call `prandgen.x`. The same code is used to randomize the position of the impurities within a certain layer to model disorder.

For transport perpendicular to (001) plane, the 5×5 supercell area A and inter-plane distance d are, respectively,

$$A = 25 \times \frac{1}{2}a^2, \text{ and } d = a. \tag{4.1}$$

For transport perpendicular to (111) plane, the 5×5 supercell area A and inter-plane distance a are given by

$$A = 25 \times \frac{\sqrt{3}}{4}a^2, \text{ and } d = \frac{\sqrt{3}}{3}a. \tag{4.2}$$

The lattice constants and related parameters that we used in this work are listed in Table 4.1.

Table 4.1: Parameters used in calculations.

Systems	z-axis	a (Å)	d (Å)	A (nm^2)
Cu-rich Co-Cu alloys	[001]	3.614	3.614	1.629
Cu-rich Co-Cu alloys	[111]	3.614	2.087	1.411
Co-rich Co-Cu alloys	[111]	3.549	2.049	1.364
$Co_{50}Cu_{50}$	[111]	3.582	2.068	1.389
Co|Cu multilayers	[111]	3.582	2.068	1.389

Before doing transport calculations, we need the effective potentials of the lead|scattering region|lead interfacial structure, which are obtained with self-consistent DFT calculations using TB-LMTO basis. Fast convergence can be achieved with good initial potentials, so we perform three steps to get the effective potentials for transport structures (CoCu alloys and multilayers). (1) We calculate the potentials of single Co and Cu atoms. (2) With the atomic potentials as an input, the bulk potentials in fcc Co and Cu are calculated self-consistently. The first two steps converge fast because the system is small. (3) Finally, we take the bulk potentials at the corresponding sites in the scattering structure and solve the Kohn-Sham equation self-consistently. Bulk potentials are applied to describe the semi-infinite leads, which do not depend on the structure/potentials in the scattering region. The coherent-potential approximation is used to mimic the impurities within alloys and at the Co|Cu interfaces (constructed of two atomic layers of 50%:50% Co-Cu mixing). Using the transport code, which employs wavefunction matching method, the total conductance of the entire structure (after being lengthened by `prandgen.x`) is computed.

4.1.2 Model and Parameters

The output from the transport code is a 2×2 conductance matrix G in the unit of the quantum conductance $\frac{e^2}{h}$ per area of one supercell A. Without SOC, the G matrix is diagonal since there is no coupling between the two channels,

$$G = \begin{pmatrix} G_{\uparrow\uparrow} & 0 \\ 0 & G_{\downarrow\downarrow} \end{pmatrix}. \tag{4.3}$$

Then the two spin channels are simply:

$$G_{\uparrow} = G_{\uparrow\uparrow}, \tag{4.4}$$

$$G_{\downarrow} = G_{\downarrow\downarrow}. \tag{4.5}$$

In the presence of SOC, the 2×2 conductance matrix is no longer diagonal due to the coupling between the two spin channels,

$$G = \begin{pmatrix} G_{\uparrow\uparrow} & G_{\uparrow\downarrow} \\ G_{\downarrow\uparrow} & G_{\downarrow\downarrow} \end{pmatrix}. \tag{4.6}$$

In this case, we define the conductance of each channels as:

$$G_{\uparrow} = G_{\uparrow\uparrow} + G_{\uparrow\downarrow}, \tag{4.7}$$

$$G_{\downarrow} = G_{\downarrow\uparrow} + G_{\downarrow\downarrow}. \tag{4.8}$$

Then we are able to define the corresponding area resistance

$$AR_{\uparrow(\downarrow)} = \frac{h}{e^2} \left(\frac{G_{\uparrow(\downarrow)}}{A} \right)^{-1}. \tag{4.9}$$

In practice, we calculate AR as a function of the length of scattering region L. At large L, AR would show a linear dependence on L following Ohm's law so that we can get the slope of the linear function. If the scattering region is an alloy, the slope (after some unit transformation) corresponds to its resistivity while the intercept arises from Sharvin resistance of leads, interface contributions between leads and scattering region. For the case of multilayers with only interface disorder, the slope corresponds to the resistance per one interface. Finally, for the case of multilayers with both interface and bulk disorder, the slope corresponds to the resistance due to both the interface and the bulk layer.

The total resistance (both with and without SOC) can be obtained from the two separate resistances using the summing rule for two resistors in parallel.

$$AR_{\text{total}} = \left(\frac{1}{AR_{\uparrow}} + \frac{1}{AR_{\downarrow}} \right)^{-1}. \tag{4.10}$$

The error of the total resistance ΔAR_{total} is also calculated from the standard deviations of the two separate channels ($\Delta AR_{\uparrow}$ and $\Delta AR_{\downarrow}$) as follows:

$$\Delta AR_{\text{total}} = \sqrt{\left(\frac{\partial AR_{\text{total}}}{\partial AR_{\uparrow}} \right)^2 (\Delta AR_{\uparrow})^2 + \left(\frac{\partial AR_{\text{total}}}{\partial AR_{\downarrow}} \right)^2 (\Delta AR_{\downarrow})^2}. \tag{4.11}$$

4.1.3 Convergence Verification

For every calculation, we need to check the convergence of k-point sampling, number of configurations, *etc.* Here we use the total conductance of Cu with 4% Co impurities as an example to show convergence verification. Transport is along [001] direction in this case. Figure 4.1 shows the calculated total conductance G (in unit of e^2/h) as a function of number of k-points in the 2D Brillouin zone for one configuration. G is plotted against the inverse of the number of k-points in order to better see the convergence as the number of k-points increases. The total conductance converges to about 0.1% with a k-point grid 32×32 in the 2D Brillouin zone so such a k-point grid is used in the all the calculations.

Once the k-point grid is fixed to be 32×32, the average of total conductance G and its standard deviation are calculated as a function of number of configurations and are plotted in Fig. 4.2. We can see that the averaged value and the error bar converge at around 10 configurations, so for all calculations we choose 10 random configurations to calculate the average conductance and its error bar.

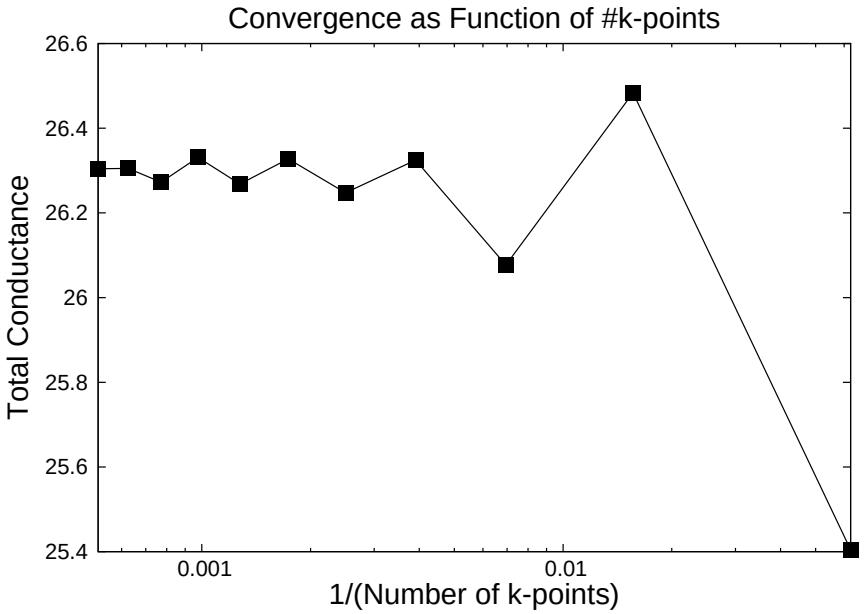

Figure 4.1: Convergence of total conductance (in unit of e^2/h) as a function of number of k-points for one configuration.

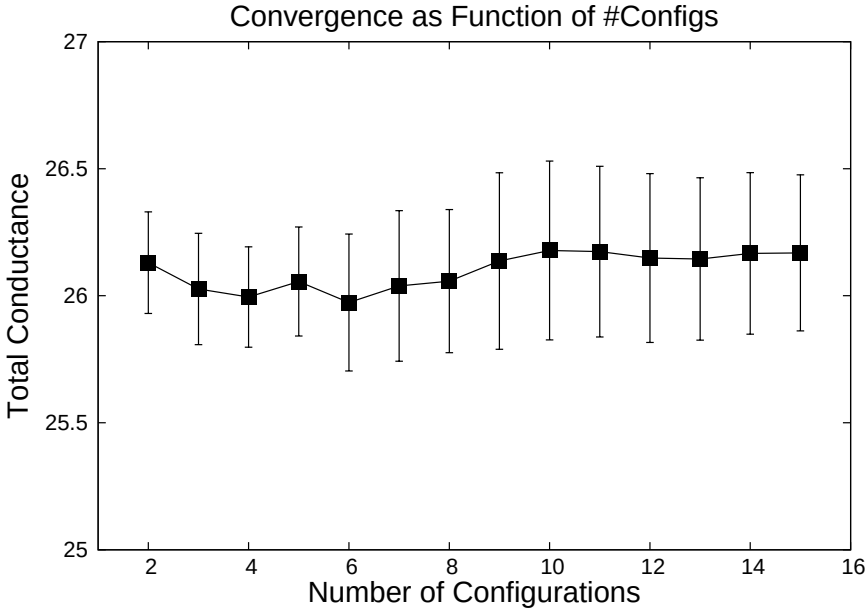

Figure 4.2: Convergence of total conductance (in unit of e^2/h) as a function of number of configurations.

4.2 Results and discussions

4.2.1 Bulk Resistivity

MSU group reported that Cu in their Co|Cu multilayer sample contributed a bulk resistivity of 0.7±0.1 $\mu\Omega$ cm at low temperature [2]. If we assume that the resistivity arises from the fact that Co atoms diffuse into Cu layers during the sputtering process, we will estimate in this section how much concentration of Co atoms corresponds to such a resistivity.

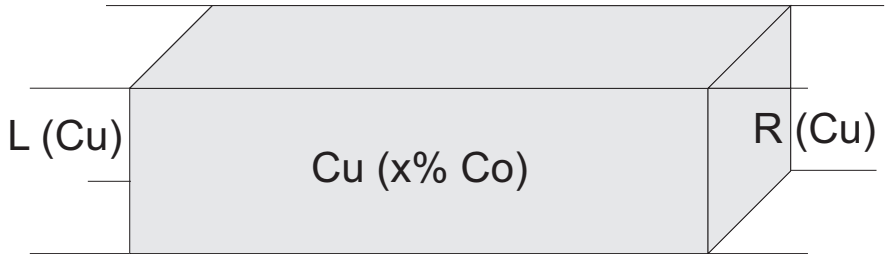

Figure 4.3: A typical structure used in transport calculation: Finite scattering region sandwiched between two Cu leads. The scattering region in this case is Cu-rich Co-Cu alloy with Co impurities.

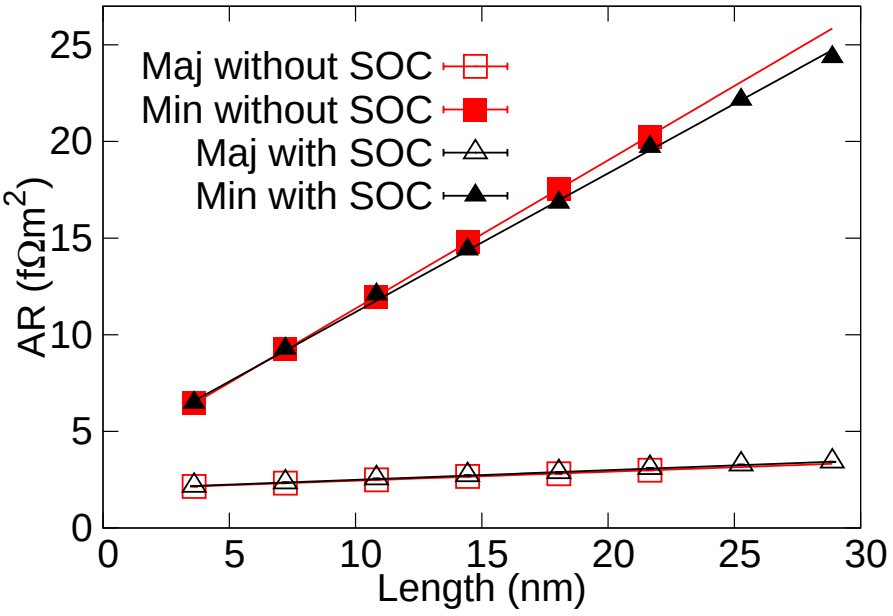

Figure 4.4: Area resistances of majority and minority spin channels of Cu-rich Co-Cu alloy (4% of Co) with and without SOC along transport direction perpendicular to [001] planes.

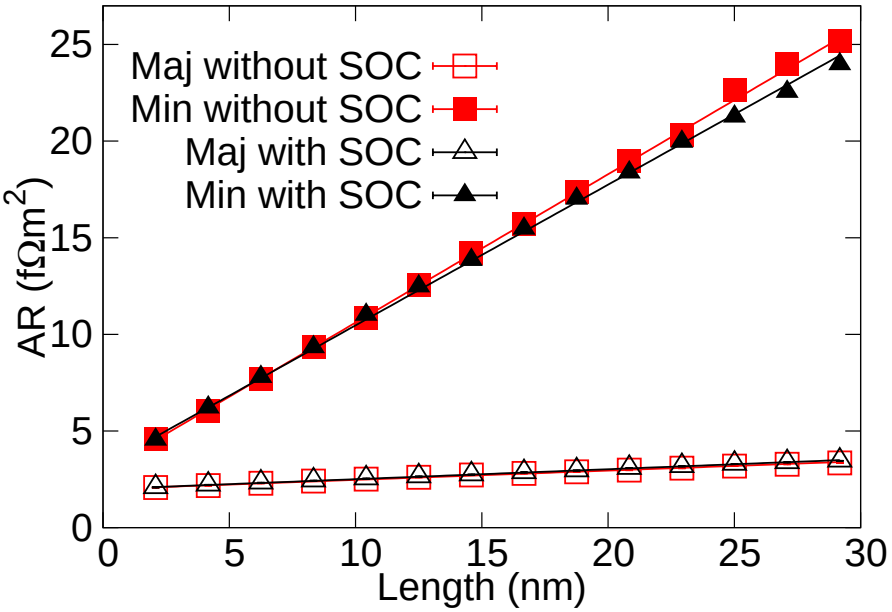

Figure 4.5: Area resistances of majority and minority spin channels of Cu-rich Co-Cu alloy (4% of Co) with and without SOC along transport direction perpendicular to [111] planes.

To calculate bulk resistivity of Cu, a finite length of Cu with a certain concentration of Co impurities is sandwiched between two pure Cu leads, as sketched in Fig. 4.3. Note that only a few percent impurities make the system diffusive, recovering the expected Ohmic behavior, i.e. the resistance shows a linear dependence on the length of the scattering region. Thus the resistivity can be extracted by a linear fit. Figure 4.4 and 4.5 show the resistance of Cu containing 4% Co impurities as a function of length along [001] and [111] directions, respectively. At every length, we have calculated about 10 random configurations and taken the standard deviation as the error, but they are too small to be visible in the figures.

Table 4.2: Resistivities of Cu with Co impurities. (Units: $\mu\Omega\,\mathrm{cm}$)

	[001]	[001]	[111]	[111]	[111]
x% Co	4%	4%	4%	4%	0.4%
SOC	No	Yes	No	Yes	No
$\rho_\uparrow$	4.6 ± 0.1	4.99 ± 0.06	4.70 ± 0.06	5.15 ± 0.05	0.93 ± 0.02
$\rho_\downarrow$	76.3 ± 0.4	71.8 ± 0.9	77.3 ± 0.6	72.8 ± 0.6	1.49 ± 0.04
ρ_{total}	4.34 ± 0.09	4.67 ± 0.05	4.43 ± 0.05	4.81 ± 0.04	0.57 ± 0.01

The extracted resistivities are listed in Table 4.2, from which we find the following infor-

mation. (1) For all cases, the majority channel has a much lower resistivity than the minority channel. It is because for majority spin all $3d$ electrons are occupied in both Cu and Co such that their majority potentials match well; but in the minority channel, they have quite different potentials resulting in a larger resistivity. (2) The resistivity has very little orientation dependence in such systems because Cu has an isotropic Fermi surface. It is not changed much by the dilute impurities of Co atoms. (3) SOC only increases the total resistivity less than 10% in contrast to the factor of 4 in $Ni_{80}Fe_{20}$ alloys. This is due to the fact that electronic states of Cu at the Fermi level have mostly s characters, for which SOC has no effect. (4) The Co concentration 0.4% gives rise to a comparable resistivity observed in MSU experiments, confirming that they made quite clean Cu layers.

Table 4.3: Resistivities of Co with 4%, 10%, 12% and 50% Cu impurities. The transport direction is along [111] in all the calculations. (Units: $\mu\Omega\,\mathrm{cm}$)

x% Cu	4%	4%	10%	12%	50%
SOC	No	Yes	Yes	Yes	Yes
$\rho_\uparrow$	1.11 ± 0.01	2.04 ± 0.02	3.96 ± 0.04	4.29 ± 0.03	10.83 ± 0.05
$\rho_\downarrow$	27.3 ± 0.2	25.1 ± 0.4	42.9 ± 0.8	36.2 ± 0.8	129 ± 5
ρ_{total}	1.07 ± 0.01	1.89 ± 0.02	3.63 ± 0.03	3.84 ± 0.03	9.99 ± 0.05

We have also calculated the resistivities of Co with Cu impurities for the concentrations 4%, 10%, 12% and 50%, respectively. The results are listed in Table 4.3. Different from the Cu-rich alloys, for Co with 4% Cu, SOC increases the total resistivity significantly. Because of the many d-bands crossing the Fermi level in Co, SOC has relatively large effects in mixing the two spin channels. Comparing to the reported bulk resistivity of Co by the MSU group about 6 $\mu\Omega\,\mathrm{cm}$, we find that the impurity concentration of Cu is larger than 12% if we assume no other types of disorder.

4.2.2 Bulk spin asymmetry coefficient β

The bulk spin asymmetry describes the ratio between majority and minority electric conductivities (resistivities),

$$\beta \equiv \frac{\sigma_\uparrow - \sigma_\downarrow}{\sigma_\uparrow + \sigma_\downarrow} = \frac{\rho_\downarrow - \rho_\uparrow}{\rho_\downarrow + \rho_\uparrow}. \tag{4.12}$$

or equivalently,

$$\rho_\uparrow = 2\rho_{\mathrm{total}}(1 - \beta), \tag{4.13}$$

$$\rho_\downarrow = 2\rho_{\mathrm{total}}(1 + \beta). \tag{4.14}$$

Without SOC, the two channels are decomposed and β can be determined unambiguously from the spin-dependent resistivities, e.g. for Co with 4% Cu, $\beta = 0.922 \pm 0.001$.

Table 4.4: Bulk spin asymmetry coefficient β of Co with varying concentration of Cu impurities determined from $\rho_\uparrow$ and $\rho_\downarrow$. The calculations are performed with SOC.

x % Cu in Co	β
4%	0.850 ± 0.003
10%	0.831 ± 0.003
50%	0.851 ± 0.005

In the presence of SOC, the two spin channels are coupled to each other via spin-flip scattering $G_{\uparrow\downarrow}$ and $G_{\downarrow\uparrow}$. Using the notation defined in previous chapters, we can still define the resistivities for the two spin channels $\rho_\uparrow$, $\rho_\downarrow$. Then we are able to determine β by applying Eq. (4.12). The bulk spin asymmetry obtained this way are listed in Table 4.4. Note that in such a scheme, we obtain β from the asymptotic $\rho_\uparrow$, $\rho_\downarrow$ at large scattering region without knowing the spin diffusion length.

Starikov *et al.* developed a method to determine β and spin-flip diffusion length $l_{\rm sf}$ simultaneously [17] by fitting the following function,

$$p^{\uparrow(\downarrow)}(z) = \frac{1}{2} \pm \frac{\beta}{2}\left[1 - \frac{\exp(-z/l_{\rm sf}) r^*_{\rm if}(\beta - \gamma + \gamma\delta)}{\beta(r^*_{\rm if} + l_{\rm sf}\delta\rho^*_F \tanh\,\delta)}\right], \tag{4.15}$$

where $\beta = (\rho_\downarrow - \rho_\uparrow)/(\rho_\downarrow + \rho_\uparrow)$ is the bulk spin asymmetry coefficient, $p^{\uparrow(\downarrow)}(z) = J^{\uparrow(\downarrow)}(z)/J$ are the fractional spin currents (with $J^{\uparrow(\downarrow)}(z)$ is the current density of majority and minority electrons, respectively), $l_{\rm sf}$ is the spin diffusion length in Co, $\rho^*_F = (\rho_\uparrow + \rho_\downarrow)/4$ is the effective bulk resistivity, $r^*_{\rm if} = (r^\uparrow_{\rm if} + r^\downarrow_{\rm if})/4$ is the effective interface resistance, $\gamma = (r^\downarrow_{\rm if} - r^\uparrow_{\rm if})/(r^\downarrow_{\rm if} + r^\uparrow_{\rm if})$ is the interface spin asymmetry coefficient.

We perform such a fitting to find β and $l_{\rm sf}$ for Co-rich alloys, as plotted in Fig. 4.6, where we take $p^{\uparrow(\downarrow)} = G_{\uparrow(\downarrow)}/G_{\rm total}$. β that are obtained by such a fitting are given in Table 4.5. It is interesting to note that the two methods lead to different values of β. The asymptotic resistivity yields β insensitive to the Cu concentration, while the fitted β using Eq. (4.15) increases with the impurity concentration. The difference between the two methods will be discussed later.

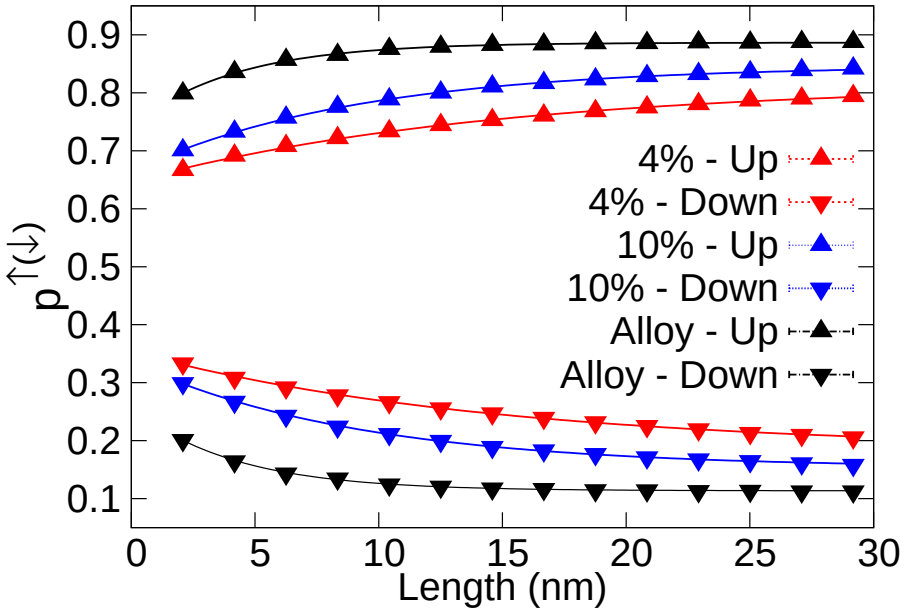

Figure 4.6: Spin fractional currents vs length to extract β of Co-rich Co-Cu alloy with varying concentration of Cu impurities.

Table 4.5: Bulk spin asymmetry coefficient β of Co with varying concentration of Cu impurities obtained using Eq. (4.15). The calculations are performed with SOC.

x%Cu	β
4 %	0.631 ± 0.007
10 %	0.694 ± 0.002
50 %	0.773 ± 0.001

4.2.3 CPP-Co|Cu multilayers

The Co|Cu multilayer structure with current perpendicular to plane (CPP) is schematically shown in Fig. 4.7, consisting of single-domain ferromagnetic Co alternating with non-magnetic Cu. The conductance per unit area G/A or area resistance AR of this system is calculated for two configurations: parallel configuration (P) and anti-parallel (AP) configuration, which means the magnetizations of neighboring ferromagnetic (Co) layers are parallel or anti-parallel, respectively.

For both P and AP cases, the two spin channels are re-labelled as $(+)$ and $(-)$ instead of $(\uparrow)$ and $(\downarrow)$ according to their absolute orientations. In this case, the two channels have approximately the same resistance: $AR_+ \approx AR_-$, hence the total resistance is approximately

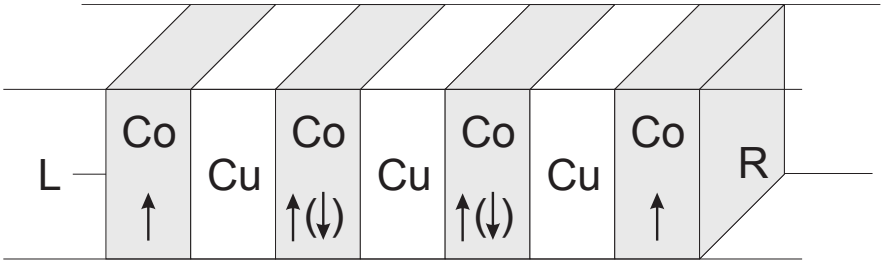

Figure 4.7: Geometry of CPP Co|Cu multilayers.

half that of each channel. For all AP cases below, the total resistance can be fitted to a line almost perfectly. For P cases, the resistances in the two channel differ considerably and the low-resistance channel dominates the total resistance due to the parallel connection.

We consider two types of Co|Cu multilayers in our calculations. The first one consists of clean Co and Cu layers with only substitutional disorder at each interface. It is modelled by randomly interchanging Co and Cu to construct two atomic layers of $Co_{50}Cu_{50}$ alloy at the interface. The second system contains not only the above interface disorder, but also includes 12% Cu impurities in Co layers to create the resistivity of ferromagnetic layers. Two different layer lengths: $t_{\mathrm{Co}} = t_{\mathrm{Cu}} = 1.034nm$ and $t_{\mathrm{Co}} = t_{\mathrm{Cu}} = 2.068nm$ were used in both types of multilayers.

4.2.4 With only interface disorder

With only interface disorder, the area resistances are obtained from linear fit of Figs. 4.8 and 4.9. Without SOC, the two spin channels have the resistances perfectly linear with the number of bilayers N. For P cases including SOC, the spin-flip scattering couples the two channels and curvatures appear for short length so we fit AR at large N where Ohmic behavior is recovered. The area resistances per bilayer are listed in Table 4.6 without SOC and in Table 4.7 with SOC included in the calculations.

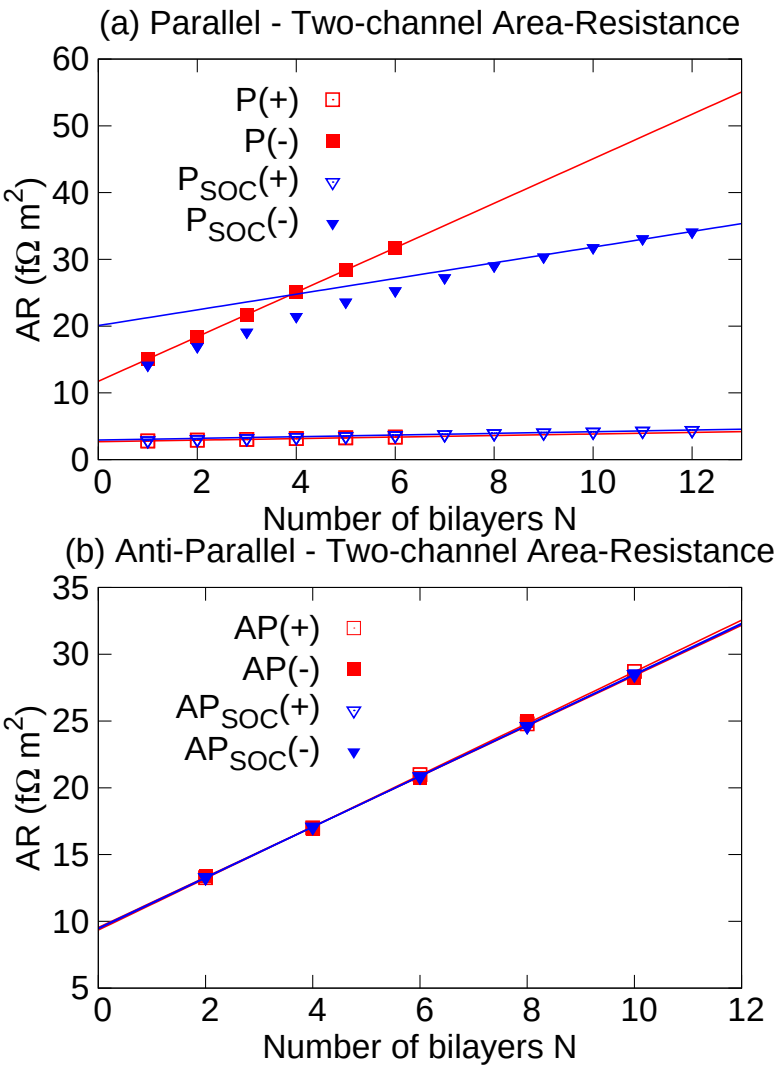

Figure 4.8: *With only interface disorder:* Two-channel area resistances of (a) Parallel and (b) Anti-parallel for each spin channel with and without SOC ($t_{\mathrm{Co}} = t_{\mathrm{Cu}} = 1.034\,\mathrm{nm}$). The figure is plotted with error bars that are smaller than the markers.

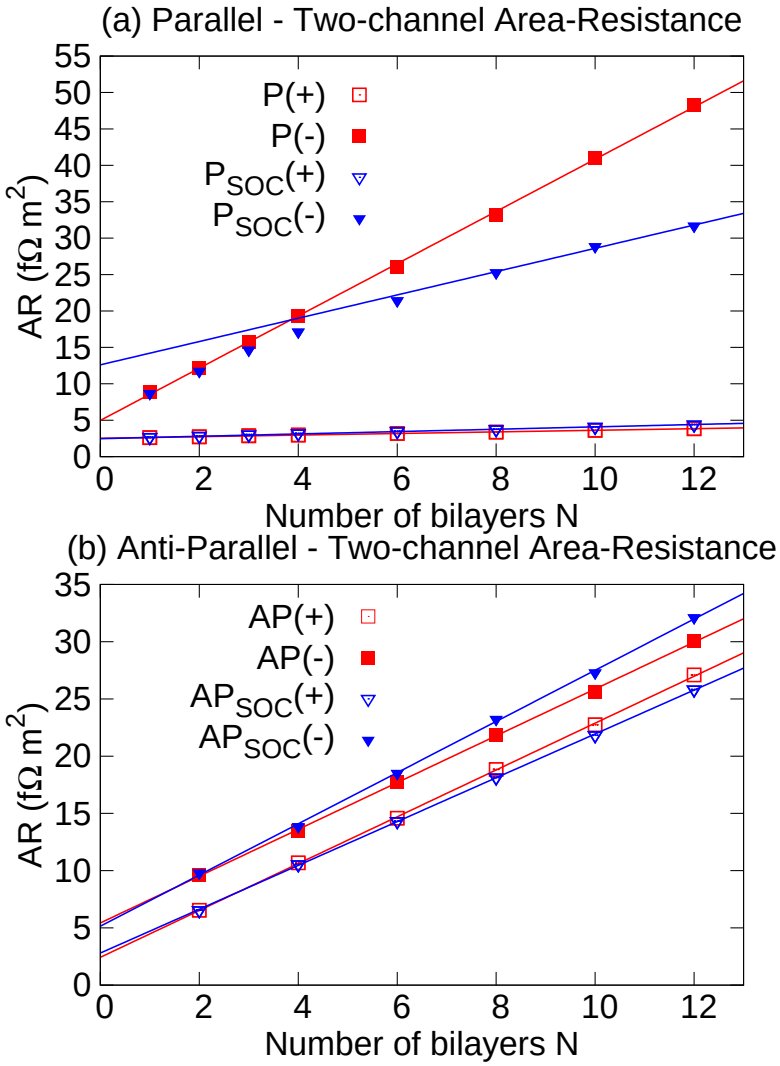

Figure 4.9: *With only interface disorder:* Two-channel area resistances of (a) Parallel and (b) Anti-parallel for each spin channel with and without SOC ($t_{\mathrm{Co}} = t_{\mathrm{Cu}} = 2.068\,\mathrm{nm}$). The figure is plotted with error bars that are smaller than the markers.

In the case of clean bulk (no impurities in the bulk layers of the multilayers) and only interface disorder due to alloying, the asymmetry in interfacial scattering between two spin channels (+ and −) can be characterized by γ, in the way similar to the bulk asymmetry scattering coefficient β above,

$$R^{+}_{F/N} = 2R_{F/N}(1 - \gamma) \tag{4.16}$$

$$R^{-}_{F/N} = 2R_{F/N}(1 + \gamma) \tag{4.17}$$

Table 4.6: Area-resistance in P and AP configurations *with only interface disorder and without SOC*.

	$t_{\mathrm{Co}} = t_{\mathrm{Cu}} = 1.034\,\mathrm{nm}$		$t_{\mathrm{Co}} = t_{\mathrm{Cu}} = 2.068\,\mathrm{nm}$	
$AR(\mathrm{f}\Omega\,\mathrm{m}^2)$	P	AP	P	AP
(+) Channel	0.12±0.002	1.93±0.01	0.11±0.002	2.046±0.014
(−) Channel	3.33±0.009	1.89±0.04	3.59±0.03	2.044±0.022
Total	0.116±0.002	0.96±0.02	0.107±0.002	1.023±0.013

Table 4.7: Area-resistance in P and AP configuration *with only interface disorder and with SOC*.

	$t_{\mathrm{Co}} = t_{\mathrm{Cu}} = 1.034\,\mathrm{nm}$		$t_{\mathrm{Co}} = t_{\mathrm{Cu}} = 2.068\,\mathrm{nm}$	
$AR(\mathrm{f}\Omega\,\mathrm{m}^2)$	P	AP	P	AP
(+) Channel	0.125±0.003	1.89±0.006	0.162±0.001	1.914±0.011
(−) Channel	1.17±0.1	1.91±0.016	1.60±0.1	2.236±0.026
Total	0.113±0.003	0.950±0.009	0.147±0.010	1.031±0.014

In the clean bulk case, the only scattering events occur at the interfaces, hence there are still two ways of extracting γ as described in Section 4.2.2:

1. Method 1: Using the definition for γ:

$$\gamma = \frac{R^{-}_{F/N} - R^{+}_{F/N}}{R^{-}_{F/N} + R^{+}_{F/N}}. \tag{4.18}$$

Using γ definition with all the relevant parameters taken from calculations gives the values in Table 4.8.

Table 4.8: Interface spin asymmetry coefficient of Co|Cu interface in P case with varying thicknesses of the layers - Method 1.

γ	$t_{Co} = t_{Cu} = 1.034\,nm$	$t_{Co} = t_{Cu} = 2.068\,nm$
Without SOC	0.930 ± 0.001	0.941 ± 0.001
With SOC	0.81 ± 0.02	0.82 ± 0.01

2. Method 2: Using the same method as [17], but letting $\gamma = \beta$. The values extracted using this method are listed in Table 4.9.

Similarly for extracting β, the two methods also gives different values of γ. We will discuss them in the next section.

Table 4.9: Interface spin asymmetry coefficient of Co/Cu interface in P case with varying thicknesses of the layers - Method 2.

γ	$t_{Co} = t_{Cu} = 1.034\,nm$	$t_{Co} = t_{Cu} = 2.068\,nm$
Without SOC	0.852 ± 0.004	0.861 ± 0.004
With SOC	0.774 ± 0.001	0.760 ± 0.001

4.2.5 With both interface and bulk disorder

In this section, we introduce disorder to the ferromagnetic layers since the MSU group reported that the ferromagnetic layers have a significant resistivity (up to 6 $\mu\Omega\,$cm at low temperature). With Cu impurities (12%) introduced in the Co layers in the CPP calculation, the total area-resistance per bilayer AR contains contributions from both the interface resistance and the bulk resistivity. We plot the total resistance as a function of N in Fig. 4.10 for $t_{\mathrm{Co}} = t_{\mathrm{Cu}} = 1.034$ nm and Fig. 4.11 for $t_{\mathrm{Co}} = t_{\mathrm{Cu}} = 2.068$ nm. The calculated AR are given in Table 4.10 without SOC and Table 4.11 with SOC.

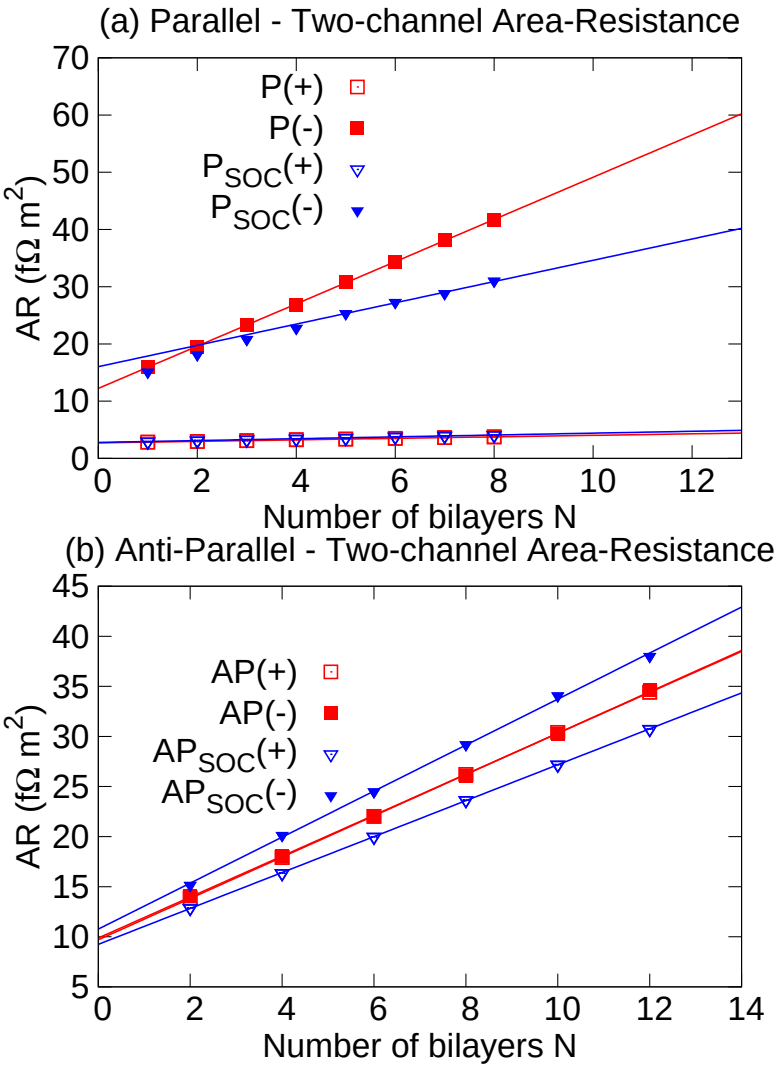

Figure 4.10: *With both bulk and interface disorder:* Two-channel area resistances of (a) Parallel and (b) Anti-parallel for each spin channel with and without SOC ($t_{\mathrm{Co}} = t_{\mathrm{Cu}} = 1.034\,\mathrm{nm}$). The figure is plotted with error bars that are smaller than the markers.

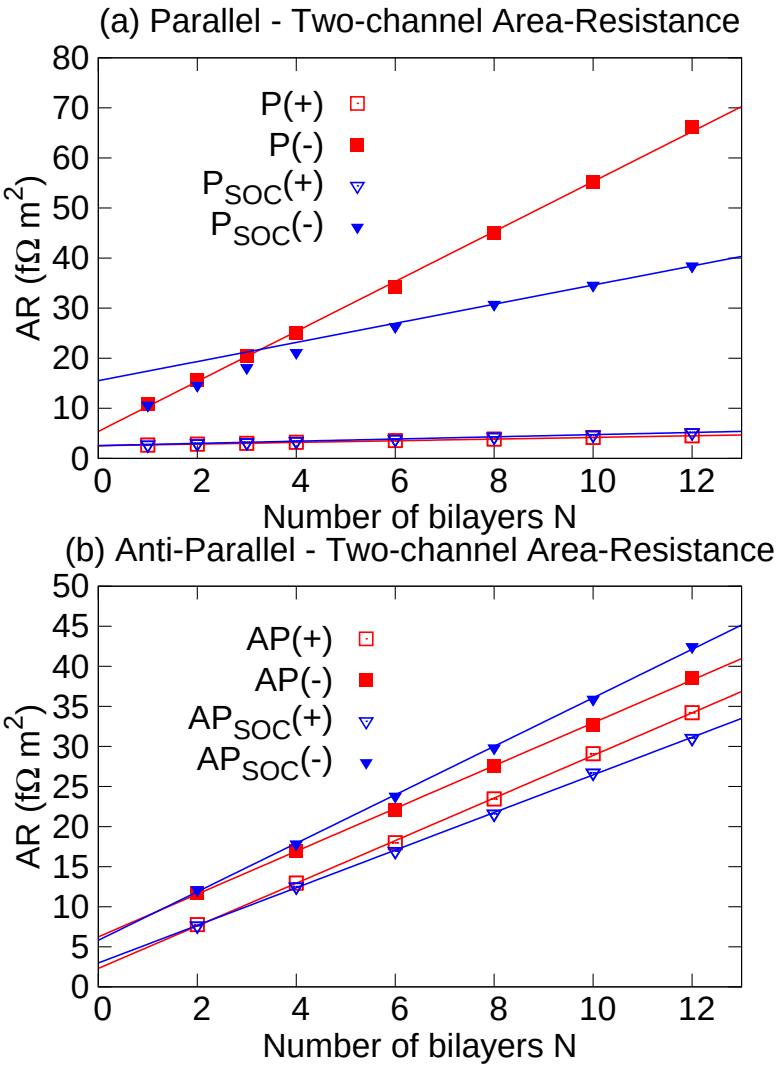

Figure 4.11: *With both bulk and interface disorder:* Two-channel area resistances of (a) Parallel and (b) Anti-parallel for each spin channel with and without SOC ($t_{\mathrm{Co}} = t_{\mathrm{Cu}} = 2.068\,\mathrm{nm}$). The figure is plotted with error bars that are smaller than the markers.

Table 4.10: Area-Resistances in P and AP configuration *with both bulk and interface disorder without SOC.*

	$t_{\mathrm{Co}} = t_{\mathrm{Cu}} = 1.034\,\mathrm{nm}$		$t_{\mathrm{Co}} = t_{\mathrm{Cu}} = 2.068\,\mathrm{nm}$	
$AR\,(\mathrm{f\Omega m^2})$	P	AP	P	AP
(+) Channel	0.132±0.003	2.063±0.007	0.166 ± 0.002	2.66 ± 0.02
(−) Channel	3.691±0.020	2.043±0.02	4.99 ± 0.06	2.67 ± 0.02
Total	0.127±0.003	1.026±0.011	0.161±0.003	1.332±0.014

Table 4.11: Area resistances in P and AP configuration *with both bulk and interface disorder with SOC.*

	$t_{\mathrm{Co}} = t_{\mathrm{Cu}} = 1.034\,\mathrm{nm}$		$t_{\mathrm{Co}} = t_{\mathrm{Cu}} = 2.068\,\mathrm{nm}$	
$AR\,(\mathrm{f\Omega m^2})$	P	AP	P	AP
(+) Channel	0.162 ± 0.007	1.793 ± 0.006	0.218 ± 0.0023	2.348 ± 0.022
(−) Channel	1.86 ± 0.01	2.297 ± 0.033	1.909 ± 0.001	3.026 ± 0.032
Total	0.149 ± 0.006	1.007 ± 0.007	0.196 ± 0.002	1.322 ± 0.009

A special problem we want to point out is that in AP cases, SOC leads to unequal AR for + and − channels. So far it has not been clear whether this is due to the spin decomposition with SOC or some symmetry breaking by SOC. It needs to be understood in the future work.

4.2.6 CPP-GMR

From the calculated area resistance, we are able to estimate the giant magnetoresistance (GMR) ratio of electronic transport in such CPP Co|Cu multilayers and to verify the influence from SOC and impurities in ferromagnetic Co layers. We use the definition of GMR ratio as

$$\mathrm{GMR} = \frac{AR_{\mathrm{AP}} - AR_{\mathrm{P}}}{AR_{\mathrm{P}}} \times 100\,\% \tag{4.19}$$

The standard propagation of errors is used to calculate the error of GMR.

$$\Delta\mathrm{GMR} = \sqrt{\left(\frac{\partial \mathrm{GMR}}{\partial AR_{\mathrm{P}}}\right)^2 (\Delta AR_{\mathrm{P}})^2 + \left(\frac{\partial \mathrm{GMR}}{\partial AR_{\mathrm{AP}}}\right)^2 (\Delta AR_{\mathrm{AP}})^2}. \tag{4.20}$$

Table 4.12: Calculated CPP GMR of Co|Cu multilayers for the cases of only interface disorder and with both interface and bulk disorder (with and without SOC)

	$t_{Co} = t_{Cu} = 1.034\,nm$		$t_{Co} = t_{Cu} = 2.068\,nm$	
$GMR\%$	Without SOC	With SOC	Without SOC	With SOC
Interface	728 ± 17	740 ± 23	856 ± 19	601 ± 10
Interface & bulk	709 ± 20	576 ± 28	728 ± 11	574 ± 8

The results are summarized in table 4.12. The lowest obtained GMR value (574±8 %) are about three times higher than the highest CPP-GMR value obtained experimentally (170 %) for the multilayered structure of $[\mathrm{Co}(1.5\,\mathrm{nm})/\mathrm{Cu}(t)]_N$, where $t \approx 1\,\mathrm{nm}$ [18].

4.3 Discussions

4.3.1 Effects of SOC on Co|Cu CPP-GMR

In Section 4.2.1, we have seen the influence of SOC in Co-Cu alloy resistivities, where the systems are always single ferromagnetic domains. SOC then introduces spin-flip scattering and couples the majority and minority spin channels, resulting in an increase in the total resistivity. The SOC strength (hence the coupling strength) is determined by the characters of electronic states at the Fermi level.

In Co|Cu multilayers, the neighboring ferromagnetic layers can be parallel or anti-parallel, and SOC has more pronounced effect in parallel configuration than in anti-parallel configuration. This is because in the former case the two spin channels (majority and minority) are clearly different: the majority channel has a much smaller resistivity compared to the minority channel. The effect of SOC is the only mechanism in coupling the two channels and increases the total resistivity, as in the alloy systems. However, in anti-parallel configuration, the two spin channels are already strongly coupled (and have comparable resistivities) so SOC has little effect. In this calculation, SOC increases AR_{P} by a factor of approximately 1.2, while leaving AR_{AP} almost unchanged.

By introducing impurities in Co layers, SOC causes spin-flip scattering not only at the interfaces but also inside ferromagnetic layers. This enhanced mixing between two conducting channels further lowers down the GMR ratio, as we see from Table 4.12. The discrepancy between our calculation and experimental observation may result from other sources of disorder besides substitutional disorder, which will be discussed in Section 4.3.4.

4.3.2 Extraction of Anisotropy Scattering coefficients β and γ

In Section 4.2.2, we described two methods to determine the bulk asymmetry coefficient β, which also apply to calculate the interface asymmetry γ. The methods yield very different results leading to the question of which one is reliable. While the results from non-linear fitting using Eq. (4.15) could be affected by the inclusion of Sharvin conductance, those obtained from spin-dependent resistivities/resistances exclude the Sharvin via the linear fitting and seem to be more reasonable.

Another support for using the parameter definition to extract the asymmetry scattering coefficient (β or γ in the clean bulk case) arises from an examination of γ for interface resistance

with only interface disorder. In this case the 2CSR model is applicable and we have :

$$\begin{aligned} AR_P &= AR_{F/N} \\ AR_{AP} &= AR^*_{F/N}. \end{aligned} \tag{4.21}$$

By definition: $AR_{F/N} = AR^*_{F/N}(1-\gamma^2)$, meaning the same as:

$$AR_{\mathrm{P}} = AR_{\mathrm{AP}}(1-\gamma^2), \tag{4.22}$$

or:

$$\gamma = \sqrt{1 - \frac{AR_{\mathrm{P}}}{AR_{\mathrm{AP}}}}, \tag{4.23}$$

It has been verified that by using γ values obtained by definition, the relation (4.22) is satisfied, whereas using γ derived from method 2 (using spin fractional current) does not satisfy (4.22). For instance, in the case of $t_{Co} = t_{Cu} = 1.034\,nm$, $AR_{\mathrm{P}} = 0.116 \pm 0.002$ f$\Omega\,$m^2, $AR_{\mathrm{AP}} = 0.96 \pm 0.02$ f$\Omega\,$m^2 in Table 4.6, using (4.23) gives $\gamma = 0.938$, consistent with the value 0.931 determined using the definition of γ (method 1), while the fitting using Eq. (4.15) gives the inconsistent $\gamma = 0.852$.

4.3.3 Comparison with the 2CSR Model

It has been established that the effective area-resistance $AR^*_{\mathrm{Co|Cu}}$ agrees well between calculations in this work and the extracted results from the measurement using the 2CSR Model, with the value of $AR^*_{\mathrm{F/N}}$ about 0.5 fΩm^2. However, other results obtained from this work showed significant differences with those extracted from the 2CSR Model for Co|Cu CPP-GMR measurements.

Given the issues with the 2CSR discussed in the previous chapter (the methods of parameter extraction, the introduction of a new parameter–spin-flip rate δ that could potentially change all the previously published values of the original 2CSR parameters), it is hard to make a meaningful comparison between the calculated parameters' values and those originally published [2, 12]. However,the comparison ought to be made just to see where our calculations stand relative to the experimental results. First among those differences is γ (approximately 0.94 without SOC and 0.82 with SOC compared to 0.76 from the 2CSR), which caused the difference in AR_{P} and subsequently GMR. Secondly, from the 2CSR model, $\rho^*_{\mathrm{Co}} = 8.6\ \mu\Omega\,$cm (and $\beta = 0.5$), a value that can only be obtained from our calculation by putting a lot of Cu impurities (more than 12%) in Co. In reality, however, such a high concentration of impurities in the

experimental samples is unlikely, and since we cannot obtain any information about the source of disorder that caused such a resistivity (or even whether this published value is accurate, since different samples give different ρ^*_{Co}). Furthermore, our calculated β values are significantly different from 0.5–Again the question arises whether 0.5 is a reliable value, since a potentially unreliable value of ρ^*_{Co} used in the extraction for β could easily lead to an unreliable β. To solve the above issues, revisiting the experimental studies is necessary, especially on the raw data instead of the extracted parameters from the 2CSR model.

4.3.4 Using Thermal Lattice Disorder in CPP Calculations

In an attempt to reproduce the experimentally reported value for ρ_{Co} of approximately 6.45 $\mu\Omega cm$ [2], we have introduced a large concentration of substitutional disorder up to 12% of Cu, which is too large to be physical. Meanwhile the calculated bulk spin asymmetry β (with just substitutional disorder)does not agree with the reported value 0.5, suggesting that other types of disorder may play a role in the multilayers. To characterize their samples, the MSU group used X-ray diffraction (XRD) analysis (the basics and details of XRD are covered in Appendix A) among other techniques, for their Co|Ag multilayer samples, where the broadening of the diffraction peaks confirmed the imperfect lattice structure in the multilayers. It is then reasonable to consider using a lattice disorder instead of, or together with substitutional disorder to reproduce the experimental Co resistivity. Liu *et al.* [19] developed a frozen thermal lattice disorder by displacing atoms randomly from their ideal lattice positions (typically by several hundredths of an angstrom). Gaussian distribution of displacements is used, characterized by the root-mean-square displacement $\Delta = \sqrt{\langle |\mathbf{u}_i|^2 \rangle}$, where the angular brackets indicate an average in which the index i runs over all atoms. This scheme can be applied in modeling the imperfect lattice of the multilayers using sputtering or other techniques at low temperature.

Previous calculation done by Liu *et al.* [19] characterizing various ferromagnetic materials' resistivities as functions of thermal lattice disorder indicates that for hcp Co at 273K (using the experimental lattice constant of 2.507 $\mathring{A}$), a rms displacement of approximately 0.1 $\mathring{A}$ corresponds to around 6.5 $\mu\Omega$cm. To make a connection with the ρ_{Co} in Co|Cu CPP-multilayers obtained in the MSU experiments in 1991, in which little information about the nature of disorder in their samples is available, we can look at their $\theta - 2\theta$ XRD spectrum on Co|Ag multilayer samples. We are interested in extracting the information from the broadened peaks, which can be translated into a rms displacement. Given the mixed character of the defects and disorder present (polycrystalline, stacking faults, strains, and combination of fcc and hcp

growth) in Co layers, which can all significantly determine the broadening of the XRD peaks, it is hard to precisely extract a small component due to lattice broadening, assuming that there is a residual lattice disorder existing in the experiments, even at a very low temperature. What can be done is to approximate the broadening of the x-ray peak entirely by an effective rms displacement using Bragg's Law of diffraction. Although this approximation might be crude, it yields a reasonable result. A rms displacement of Δ introduces a change of $\pm\Delta$ in the interplanar distance d, resulting in an interval $d \pm \Delta$ corresponding to a shift of the original X-ray peak $\theta(d)$ to an upper value of $\theta(d-\Delta)$ and a lower value of $\theta(d+\Delta)$. (Note: $\theta(d)$ is the Bragg angle corresponding to an interplanar distance d, $\theta(d+\Delta)$ is the Bragg angle corresponding to $d+\Delta$, and so on). With this, one can roughly estimate the effective rms displacement of the sample used in the experiment from XRD scan results. Using the XRD results (3.3) obtained from [10], we see that the diffraction peak of bulk Co (approximately at 44^0 in 2θ scan) has a FWHM of about 0.5^0, corresponding to an effective rms displacement of 0.02^0. This is smaller than the value obtained in [19], but it is hard to draw any conclusions from this difference, because the XRD is done on Co|Ag instead of Co|Cu samples (and ρ^*_{Co} in Co|Ag sample is different from that in Co|Cu sample, according to the published experimental values [2]).

Chapter 5

Outlook

The results of this work have shown that the influence of SOC on CPP-GMR is rather small and does not contribute towards a better agreement with experiments. Besides, the coupling mechanism of SOC on two separate spin channels in P and AP case should be further investigated, especially in AP case where the results obtained show a splitting of (+) and (−) channel. Although there are limiting uncertainties involved with past and current experimental studies, in order to better bridge the gap between theoretical calculations and experimental results, the nature of disorder in ferromagnetic layer and at the F/N interface in CPP structure should be better understood and modelled. It has been demonstrated in this thesis that substitutional disorder alone cannot reproduce the amount of resistivity and anisotropy scattering coefficient reported experimentally for Co. It is then worth considering using other types of disorder like lattice disorder and even stacking faults in Co layer (more realistically Co layer has a combination of fcc(111) and hcp(0001) domains instead of just fcc(111)) in our future calculations.

Appendix A

Basics of X-ray Diffraction (XRD)

A.1 Overview

X-ray diffraction studies of materials are important tools for probing the crystalline structure, chemical composition, and physical properties of materials and thin films. Due to the short wavelength of X-rays (0.01 nm to 10 nm), it can be use to probe the finer structures of the material with a comparable length scale. The high energy of X-rays means that excitation of the atoms in the materials can also occur. Analysis of the resulting emitted radiation can be done to extract the chemical composition of the material.

Specular scattering occurs when X-rays impinging on an atom is scattered with the same angle from the normal as the angle of incidence. When this occurs in a regular periodic structure (Fig. A.1) like a crystal, the scattered X-rays being coherent with each other will undergo interference. The condition for constructive interference is given by the Bragg's Law for diffraction:

$$n\lambda = 2d_{hkl}sin\theta \tag{A.1}$$

where n is the diffraction order, λ is the X-ray wavelength, d_{hkl} is the interplane distance, and θ is the angle between the incidence x-ray beam and the sample surface.

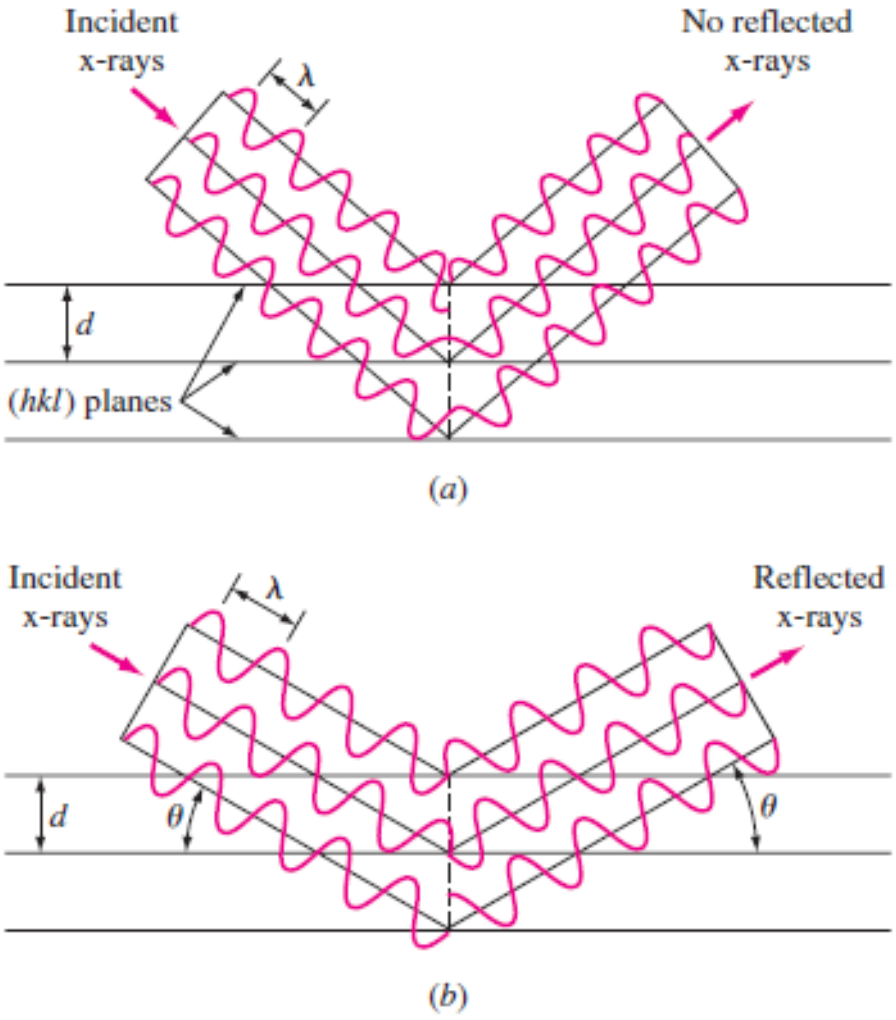

Figure A.1: Bragg's Law of diffraction.(a) Destructive interference of reflected waves at an arbitrary angle θ. (b) Constructive interference of reflected waves at a Bragg angle θ. Figures adapted from [20]

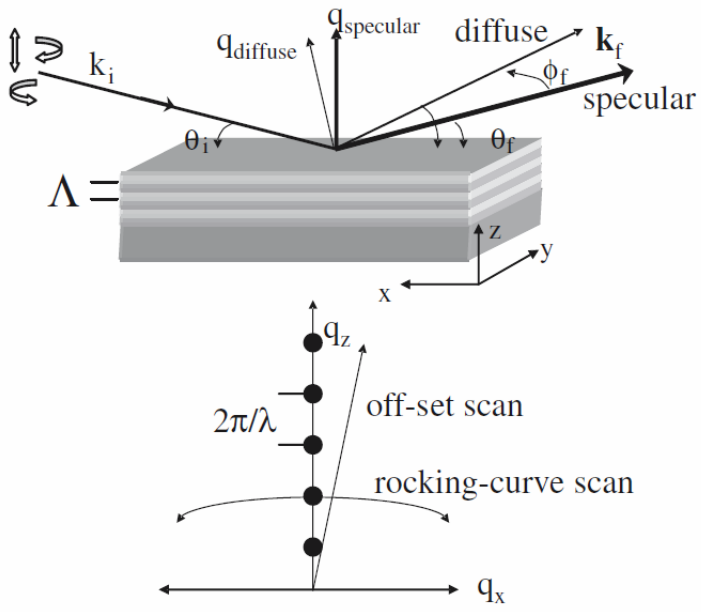

Figure A.2: Scattering geometry from a diffraction measurement on a multilayer structure with period Λ (Top). For specular scattering, $\theta_i = \theta_f$. With rough interfaces, diffused scattering occurs with $\theta_i \neq \theta_f$ and $\phi_f \neq 0$. The corresponding scattering geometry in reciprocal space (bottom) can be probed with a rocking scan. Figure adapted from [21]

As the angle of incidence and angle of reflection are equal for specular scattering (Fig.A.2), to detect the scattered X-rays, the normal of the sample surface is always placed at half of the angle between the incident X-ray beam and the line of sight of the detector. Thus this technique is known as $\theta - 2\theta$ X-ray diffraction. A typical result from an XRD scan contains peaks corresponding to angles at which the Bragg diffraction condition is satisfied.

A scan is usually done over a range of angle θ such that the Bragg diffraction condition is satisfied for both $n < 0$ and the corresponding $n > 0$. This results in two identical set of peaks on either side of the zeroth-order maximal. Thus by relating the two set of peaks, it is possible then to identify the order of the peaks n. By fitting a plot of the order n of the peaks versus the corresponding value of $\frac{2sin\theta}{\lambda}$, the value of d can be obtained.

The idealized peaks of the diffraction scan are infinitely sharp. This scenario corresponds to the case where the X-ray have infinitely narrow bandwidth, which is not true in reality. Because of the finite bandwidth of the X-rays, the full-width-half-maximum (FWHM) of the peaks get

progressively smaller when more layers are contributing to the interference. By extension, FWHM of the peaks is dependent on the number of atoms in the sample.

The $\theta - 2\theta$ scans only reveal information about the periodicity parallel to the surface of the sample. In order to probe the periodicity in other orientations, the angle between the sample normal and X-ray beam is varied while maintaining the angle between the incident X-ray beam and the line of sight of the detector. This is called a rocking curve scan (Fig.A.2).

A.2 Defects Possibly Extractable from XRD

Apart from the finite bandwidth of the X-rays used, the disorder in the sample can also lead to a broadening of the peaks. Some of the possible defects are highlighted here:

1. **Intermixing between layers:** In samples with multilayer structures, there is an intermixing of the two materials in between the monolayers. This is due to the diffusion of the two materials into each other. There is a gradual change in the lattice constant from that of one monolayer to another. The gradual change in the lattice constant implies that more sets of Bragg diffraction conditions in the XRD are satisfied for the multilayer structures, giving rise to broadened diffraction peaks.

2. **Finite crystallite size:** In reality fabricated samples are not monocrystalline. Due to growing conditions and surface defects, they may have a polycrystalline structure composing of crystallite with various size distribution and orientations. Each of this crystallite satisfy their own set of Bragg diffraction condition, giving rise to broadened peaks (Fig. A.3).

   The broadening of the the FWHM due to the finite crystallite size B_{size} is given by the Scherrer equation [22]:

   $$B_{size}\,(2\theta) \;=\; \frac{K\lambda}{L\,cos\,\theta}, \tag{A.2}$$

   where K is the Scherrer constant (typcial 0.9), L is the apparent size of the crystalline domain, and λ is the wavelength of the X-ray. Using A.2, calculation of the expected FWHM for the diffraction peak for bulk Co at $2\theta = 44°$ is made. This is shown in Fig. A.4.

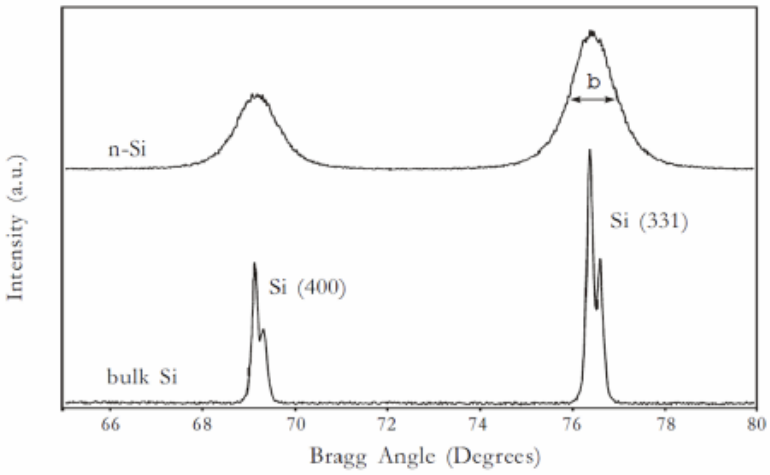

Figure A.3: Diffraction patterns of nanocrystalline Silicon showing broadening due to particle size. Figure adapted from [22]

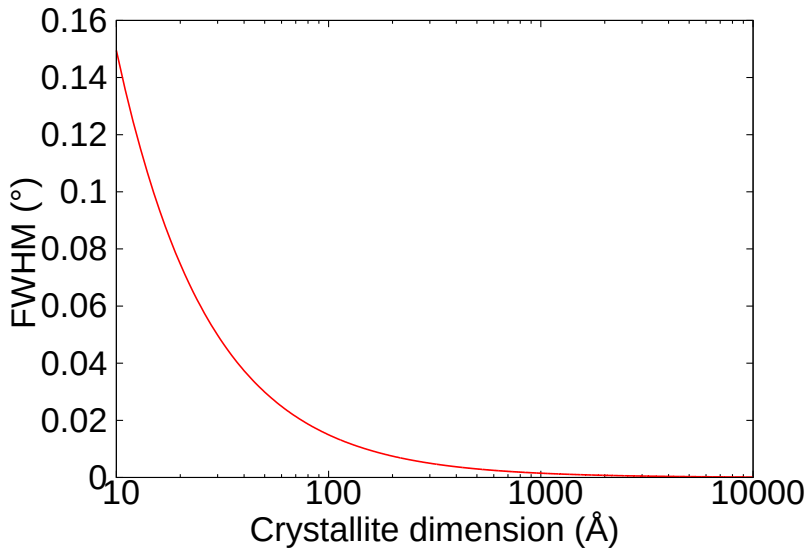

Figure A.4: A Matlab generated plot showing the dependence of bandwidth(°) on size of crystalline domain ($\mathring{A}$) for a diffraction peak of Co at $2\theta = 44°$.

3. **Interface roughness:** Thin films growth is usually uniform up to a few monolayers. After which columnar structure begin to develop. This results in surface roughness giving rise to an incoherent interface when it comes to multilayer structure. Each of the pro-

trusion in the interface give rise to its own set of Bragg diffraction condition, resulting in broadened peaks.

4. **Thermal disorder:** So far the defects mentioned are frozen-in defects which do not change over time. However, due to thermal energy, various vibrational modes in the lattice may be excited. Vibration of the lattice points results in a mean displacement from the periodic lattice points, giving rise to an irregular lattice. This results in a slightly different set of Bragg diffraction condition being satisfied, leading to broadened peaks and a different dependence on angle θ with temperature. The dependence of the intensity of the diffracted peaks on the mean square displacement $\langle u^2 \rangle$ is given by the Debye-Waller factor:

$$f = e^{-M}, \tag{A.3}$$

where

$$M = \frac{1}{2}\left(\frac{4\pi}{\lambda}\right)^2 sin^2\theta \langle u^2 \rangle . \tag{A.4}$$

To gain a qualitative understanding of the dependence of diffraction peak broadening for a given RMS displacement Δ (defined previously in Chapter 4), the corresponding angle for the diffraction peaks are evaluated using Eq. A.1 for various intervals of $[d - \Delta, d + \Delta]$ where d is the interplane distance evaluated from the diffraction peak for bulk Co at $2\theta = 44°$. The absolute difference of the angle θ obtained at these two interval then gives the width of the diffracted peak. This is shown in Fig. A.5.

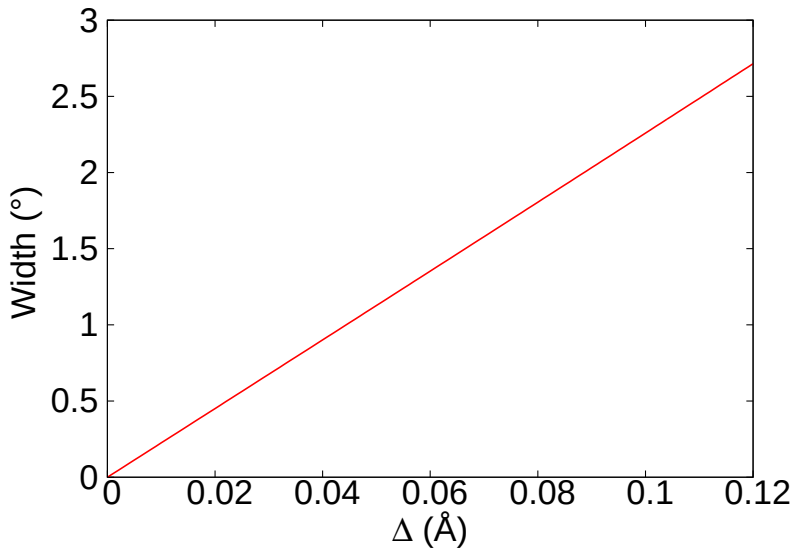

Figure A.5: A Matlab generated plot showing the dependence of width(°) on the RMS displacement Δ of the lattice points in terms of d for a diffraction peak of Co at $2\theta = 44°$.

Appendix B

Coherent vs. Incoherent Transport

B.1 Scattering Matrix of a Double Square Potential Barrier

B.1.1 Individual Scattering Matrix of Each Barrier

The scattering matrix is defined as:

$$S = \begin{pmatrix} r & t' \\ t & r' \end{pmatrix} \tag{B.1}$$

The Schrodinger equation for a double square-well potential barrier in 1D (along $\hat{z}$):

$$\left[-\frac{\hbar^2}{2m}\nabla^2 + V(z) \right] \Psi = E\Psi \tag{B.2}$$

$$V(z) = \begin{cases} 0, & z \leq 0 & \text{(I)} \\ V_1, & 0 \leq z \leq a & \text{(II)} \\ 0, & a \leq z \leq d & \text{(III)} \\ V_2, & d \leq z \leq (d+a) & \text{(IV)} \\ 0, & z \geq (d+a) & \text{(V)} \end{cases} \tag{B.3}$$

The first potential barrier consists of 3 regions (I, II, and III) and its own scattering matrix S_1

In (I): $z \leq 0, V(z) = 0$, the solution is:

$$\Psi_I = A_1 e^{ikz} + B_1 e^{-ikz} \tag{B.4}$$

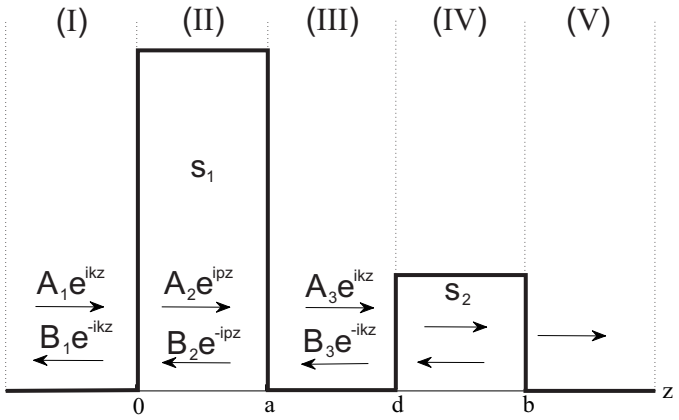

Figure B.1: Double potential barrier.

$$k = \frac{\sqrt{2mE}}{\hbar} \tag{B.5}$$

In (II): $0 \leq z \leq a, V(z) = V_0$, the solution is:

$$\Psi_{II} = A_2 e^{ipz} + B_2 e^{-ipz} \tag{B.6}$$

$$p = \frac{\sqrt{2m(E - V_1)}}{\hbar} \tag{B.7}$$

In (III): $a \leq z \leq b, V(z) = 0$, the solution is:

$$\Psi_{III} = A_3 e^{ikz} + B_3 e^{-ikz} \tag{B.8}$$

$$k = \frac{\sqrt{2mE}}{\hbar} \tag{B.9}$$

The scattering matrix S_1 can be constructed by solving a set of boundary conditions:

$$\Psi_I(0) = \Psi_{II}(0) \tag{B.10}$$

$$\frac{d\Psi_I(0)}{dz} = \frac{d\Psi_{II}(0)}{dz} \tag{B.11}$$

$$\Psi_{II}(a) = \Psi_{III}(a) \tag{B.12}$$

$$\frac{d\Psi_{II}(a)}{dz} = \frac{d\Psi_{III}(a)}{dz} \tag{B.13}$$

The explicit boundary conditions are:

$$A_1 + B_1 = A_2 + B_2 \tag{B.14}$$

$$ik(A_1 - B_1) = ip(A_2 - B_2) \tag{B.15}$$

$$(A_2 e^{ipa} + B_2 e^{-ipa}) = (A_3 e^{ika} + B_3 e^{-ika}) \tag{B.16}$$

$$ip\,(A_2 e^{ipa} - B_2 e^{-ipa}) = ik\,(A_3 e^{ika} - B_3 e^{-ika}) \tag{B.17}$$

From (B.14) and (B.15) we have:

$$A_2 = \frac{1}{2}\left[\left(\frac{k}{p}+1\right)A_1 + \left(1-\frac{k}{p}\right)B_1\right] \tag{B.18}$$

$$B_2 = \frac{1}{2}\left[\left(\frac{k}{p}+1\right)B_1 + \left(1-\frac{k}{p}\right)A_1\right] \tag{B.19}$$

Substituting (B.18) and (B.19) into (B.16) and rearranging give:

$$\begin{aligned} A_3 e^{ika} &= \frac{1}{2}\left[\left(\frac{k}{p}+1\right)A_1 + \left(1-\frac{k}{p}\right)B_1\right]e^{ipa} \\ &+ \frac{1}{2}\left[\left(\frac{k}{p}+1\right)B_1 + \left(1-\frac{k}{p}\right)A_1\right]e^{-ipa} \\ &- B_3 e^{-ika} \end{aligned} \tag{B.20}$$

Substituting (B.20), (B.18) and (B.19) into (B.17) gives:

$$\begin{aligned} & p\left(\frac{1}{2}\left[\left(\frac{k}{p}+1\right)A_1 + \left(1-\frac{k}{p}\right)B_1\right]e^{ipa} - \frac{1}{2}\left[\left(\frac{k}{p}+1\right)B_1 + \left(1-\frac{k}{p}\right)A_1\right]e^{-ipa}\right) \\ = \; & k\left(\frac{1}{2}\left[\left(\frac{k}{p}+1\right)A_1 + \left(1-\frac{k}{p}\right)B_1\right]e^{ipa} + \frac{1}{2}\left[\left(\frac{k}{p}+1\right)B_1 + \left(1-\frac{k}{p}\right)A_1\right]e^{-ipa}\right. \\ & \left. - 2B_3 e^{-ika}\right) \end{aligned} \tag{B.21}$$

Collecting terms with the same coefficients gives:

$$\begin{aligned} & \frac{1}{2}\left(\frac{p}{k}-1\right)\left(\frac{k}{p}+1\right)A_1 e^{ipa} - \frac{1}{2}\left(\frac{p}{k}+1\right)\left(1-\frac{k}{p}\right)A_1 e^{ipa} + 2B_3 e^{-ika} \\ = \; & \frac{1}{2}\left(1-\frac{k}{p}\right)\left(1-\frac{p}{k}\right)B_1 e^{ipa} + \frac{1}{2}\left(1+\frac{k}{p}\right)\left(1+\frac{p}{k}\right)B_1 e^{-ipa} \end{aligned} \tag{B.22}$$

Letting $\gamma = \frac{k}{p}$, finally, we arrive at:

$$\begin{aligned} & \left(1-\gamma^2\right)\left(e^{ipa} - e^{-ipa}\right)A_1 + 4\gamma e^{-ika}B_3 \\ = \; & \left[(1+\gamma)^2 e^{-ipa} - (1-\gamma)^2 e^{ipa}\right]B_1 \end{aligned} \tag{B.23}$$

Or, in a more suggestive form:

$$\begin{aligned} B_1 &= \frac{2i(1-\gamma^2)sin(pa)}{\left[(1+\gamma)^2 e^{-ipa} - (1-\gamma)^2 e^{ipa}\right]}A_1 \\ &+ \frac{4\gamma e^{-ika}}{\left[(1+\gamma)^2 e^{-ipa} - (1-\gamma)^2 e^{ipa}\right]}B_3 \end{aligned} \tag{B.24}$$

The transmission probability A_3 in terms of A_1 and B_3 is determined by substituting (B.24) into (B.20):

$$\begin{aligned} A_3 &= \frac{4\gamma e^{-ika}}{\left[(1+\gamma)^2 e^{-ipa} - (1-\gamma)^2 e^{ipa}\right]} A_1 \\ &+ \frac{2i(1-\gamma^2)sin(pa)e^{-2ika}}{\left[(1+\gamma)^2 e^{-ipa} - (1-\gamma)^2 e^{ipa}\right]} B_3 \end{aligned} \tag{B.25}$$

The transmitted and reflected amplitudes are related to the incoming wave amplitude via the scattering matrix s_1:

$$\begin{pmatrix} B_1 \\ A_3 \end{pmatrix} = \begin{pmatrix} r_1 & t_1' \\ t_1 & r_1' \end{pmatrix} \begin{pmatrix} A_1 \\ B_3 \end{pmatrix} \tag{B.26}$$

Therefore, the first scattering matrix associated with the first square potential barrier V_1 is:

$$\begin{aligned} s_1 = \begin{pmatrix} r_1 & t_1' \\ t_1 & r_1' \end{pmatrix} &= \frac{1}{\left[(1+\gamma)^2 e^{-ipa} - (1-\gamma)^2 e^{ipa}\right]} \times \\ &\begin{pmatrix} 2i(1-\gamma^2)sin(pa) & 4\gamma e^{-ika} \\ 4\gamma e^{-ika} & 2i(1-\gamma^2)sin(pa)e^{-2ika} \end{pmatrix} \end{aligned} \tag{B.27}$$

The second scattering matrix s_2 associated with the second square potential barrier V_2 shifted a distance d from the first potential barrier V_1 is obtained from s_1 by applying a translation operation on the latter [23]:

$$s_2 = \begin{pmatrix} r_2 & t_2' \\ t_2 & r_2' \end{pmatrix} = \begin{pmatrix} e^{2ikd} r_1 & t_1' \\ t_1 & e^{-2ikd} r_1' \end{pmatrix} \tag{B.28}$$

$$\begin{aligned} s_2 = \begin{pmatrix} r_2 & t_2' \\ t_2 & r_2' \end{pmatrix} &= \frac{1}{\left[(1+\chi)^2 e^{-iqa} - (1-\chi)^2 e^{iqa}\right]} \times \\ &\begin{pmatrix} 2ie^{2ikd}(1-\chi^2)sin(qa) & 4\chi e^{-ika} \\ 4\chi e^{-ika} & 2ie^{-2ikd}(1-\chi^2)sin(qa)e^{-2ika} \end{pmatrix} \end{aligned} \tag{B.29}$$

where $q = \frac{\sqrt{2m(E-V_2)}}{\hbar}$ and $\chi = \frac{k}{q}$

B.1.2 Combined Scattering Matrix for Incoherent Transport

Due to the complexity of treating coherent transport, incoherent transport is presented first.

For incoherent transport, the probabilities instead of the amplitudes of each individual scattering matrix is combined to form the equivalent one:

$$S_1 = \begin{pmatrix} R_1 & T_1' \\ T_1 & R_1' \end{pmatrix} \tag{B.30}$$

where $R_1 = |r_1|^2, R_1' = |r_1'|^2, T_1 = |t_1|^2, T_1' = |t_1'|^2$

$$S_2 = \begin{pmatrix} R_2 & T_2' \\ T_2 & R_2' \end{pmatrix} \tag{B.31}$$

where $R_2\,, |r_2|^2, R_2' = |r_2'|^2, T_2 = |t_2|^2, T_2' = |t_2'|^2$

The combined scattering matrix S in this case is:

$$S = \begin{pmatrix} R & T' \\ T & R' \end{pmatrix} = \begin{pmatrix} R_1 + \frac{T_1' R_2 T_1}{1 - R_1' R_2} & \frac{T_1' T_2'}{1 - R_1' R_2} \\ \frac{T_1 T_2}{1 - R_1' R_2} & R_2' + \frac{T_2 R_1' T_2'}{1 - R_1' R_2} \end{pmatrix} \tag{B.32}$$

$$T_{AP}(-) = \frac{16^2 \alpha^2 \beta^2}{16^2 \alpha^2 \beta^2 + 64\left[(1-\beta^2)^2 \alpha^2 sin^2 k_\downarrow a + (1-\alpha^2)^2 \beta^2 sin^2 k_\uparrow a\right]} \tag{B.33}$$

It can be seen from (B.56) and (B.34) that: $T_{AP}(+) = T_{AP}(-)$.

Consequently, the total transmission in AP case is:

$$\begin{aligned} T_{AP} &= 2T_{AP}(+) = 2T_{AP}(-) \\ &= \frac{2 \times 16^2 \alpha^2 \beta^2}{16^2 \alpha^2 \beta^2 64\left[(1-\beta^2)^2 \alpha^2 sin^2 k_\downarrow a + (1-\alpha^2)^2 \beta^2 sin^2 k_\uparrow a\right]} \end{aligned} \tag{B.34}$$

The transmission T is : $T = \frac{T_1 T_2}{1 - R_1' R_2}$

Substituting relevant expressions for T_1, T_2, R_1', R_2 we have:

$$\begin{aligned} T_1 &= \frac{16\gamma^2}{(1+\gamma)^4 + (1-\gamma)^4 - 2(1-\gamma^2)^2 cos(2pa)} \\ T_2 &= \frac{16\chi^2}{(1+\chi)^4 + (1-\chi)^4 - 2(1-\chi^2)^2 cos(2qa)} \\ R_1' &= \frac{4(1-\gamma^2)^2 sin^2 pa}{(1+\gamma)^4 + (1-\gamma)^4 - 2(1-\gamma^2)^2 cos(2pa)} \\ R_2 &= \frac{4(1-\chi^2)^2 sin^2 qa}{(1+\chi)^4 + (1-\chi)^4 - 2(1-\chi^2)^2 cos(2qa)} \end{aligned}$$

The explicit expression for T is better presented separately (numerator and denominator): $T = \frac{T_N}{T_D}$ where:

$$T_N = 16^2 \gamma^2 \chi^2 \tag{B.35}$$

$$\begin{aligned} T_D &= \left[(1+\gamma)^4 + (1-\gamma)^4 - 2(1-\gamma^2)^2 cos(2pa)\right] \\ &\times \left[(1+\chi)^4 + (1-\chi)^4 - 2(1-\chi^2)^2 cos(2qa)\right] \\ &- 16(1-\gamma^2)^2 (1-\chi^2)^2 sin^2(pa) sin^2(qb) \end{aligned} \tag{B.36}$$

$$\begin{aligned} T_D &= (1+\gamma)^4(1+\chi)^4 + (1-\gamma)^4(1+\chi)^4 \\ &+ (1+\gamma)^4(1-\chi)^4 + (1-\gamma)^4(1-\chi)^4 \\ &- 2(1-\gamma^2)^2 cos(2pa)\left((1+\chi)^4 + (1-\chi)^4\right) \\ &- 2(1-\chi^2)^2 cos(2qa)\left((1+\gamma)^4 + (1-\gamma)^4\right) \\ &+ 4(1-\gamma^2)^2(1-\chi^2)^2 cos(2pa)cos(2qa) \\ &- 16(1-\gamma^2)^2(1-\chi^2)^2 sin^2(pa)sin^2(qa) \end{aligned} \tag{B.37}$$

Using the following:

$$\begin{aligned} cos2\theta &= 1 - 2sin^2\theta\left[(1-\gamma)^2 - (1+\gamma)^2\right]^2 \\ &= 16\gamma^2(1-\gamma)^4 + (1+\gamma)^4 \\ &= 2(1-\gamma^2)^2 + 16\gamma^2 \end{aligned} \tag{B.38}$$

and manipulating T_D finally give:

$$T_D = 16^2\gamma^2\chi^2 + 64[(1-\gamma^2)^2\chi^2 sin^2 pa + (1-\chi^2)^2\gamma^2 sin^2 qa] \tag{B.39}$$

From(B.35) and (B.39), the transmission coefficient for incoherent transport through double square potential barriers ($V_1 \neq V_2$) is:

$$T = \frac{16^2\gamma^2\chi^2}{16^2\gamma^2\chi^2 + 64[(1-\gamma^2)^2\chi^2 sin^2 pa + (1-\chi^2)^2\gamma^2 sin^2 qa]} \tag{B.40}$$

B.1.3 Combined Scattering Matrix for Coherent Transport

For coherent transport, the combined scattering matrix s from s_1 and s_2 is [24]:

$$s = \begin{pmatrix} r & t' \\ t & r' \end{pmatrix} = \begin{pmatrix} r_1 + \frac{t_1' r_2 t_1}{1 - r_1' r_2} & \frac{t_1' t_2'}{1 - r_1' r_2} \\ \frac{t_1 t_2}{1 - r_1' r_2} & r_2' + \frac{t_2 r_1' t_2'}{1 - r_1' r_2} \end{pmatrix} \tag{B.41}$$

For our purpose of analyzing the total resistance or total conductance of a multilayer system, which is related to the total transmission probability $|t|^2$ as $G = \frac{e^2}{h}|t|^2$ (considering only one transport mode), we are only interested in the t element of the combined scattering matrix, which can be extracted from the matrix above as:

$$T = |t|^2 = \left|\frac{t_1 t_2}{1 - r_1' r_2}\right|^2 \tag{B.42}$$

Substituting the explicit expression for each elements (t_1, t_2, r_1', r_2) into (B.42), and multiplying the whole expression with its complex conjugate, one obtains the explicit expression for T

(separated into its numerator T_N and denominator T_D due to its complexity):

$$T_N = |t_1 t_2|^2 = (16\gamma\chi)^2 \tag{B.43}$$

$$T_D = |1 - r_1' r_2|^2 = AB + C + (D + E) \tag{B.44}$$

$$\begin{aligned}
AB &= \left[(1+\gamma)^2 e^{-ipa} - (1-\gamma)^2 e^{ipa}\right]\left[(1+\gamma)^2 e^{ipa} - (1-\gamma)^2 e^{-ipa}\right] \\
&\times \left[(1+\chi)^2 e^{-iqa} - (1-\chi)^2 e^{iqa}\right]\left[(1+\chi)^2 e^{+iqa} - (1-\chi)^2 e^{-iqa}\right] \\
&= (1+\gamma)^4(1+\chi)^4 + (1-\gamma)^4(1+\chi)^4 \\
&+ (1+\gamma)^4(1-\chi)^4 + (1-\gamma)^4(1-\chi)^4 \\
&- 2(1-\gamma^2)^2 cos(2pa)\left((1+\chi)^4 + (1-\chi)^4\right) \\
&- 2(1-\chi^2)^2 cos(2qa)\left((1+\gamma)^4 + (1-\gamma)^4\right) \\
&+ 4(1-\gamma^2)^2(1-\chi^2)^2 cos(2pa)cos(2qa) \\
&= 16^2\gamma^2\chi^2 + 64[(1-\gamma^2)^2\chi^2 sin^2 pa + (1-\chi^2)^2\gamma^2 sin^2 qa] \\
&+ 16(1-\gamma^2)^2(1-\chi^2)^2 sin^2(pa) sin^2(qa)
\end{aligned} \tag{B.45}$$

$$C = 16(1-\gamma^2)^2(1-\chi^2)^2 sin^2(pa) sin^2(qa) \tag{B.46}$$

$$\begin{aligned}
D + E &= 4(1-\gamma^2)^2(1-\chi^2)^2 sin(pa) sin(qa) \times F \\
&= 2(1-\gamma^2)^2(1-\chi^2)^2 \left[cos\, a(p-q) - cos\, a(q+p)\right] \times F
\end{aligned} \tag{B.47}$$

$$\begin{aligned}
F &= e^{2ik(a-d)}\left[(1+\gamma)^2 e^{-ipa} - (1-\gamma)^2 e^{ipa}\right]\left[(1+\chi)^2 e^{-iqa} - (1-\chi)^2 e^{iqa}\right] \\
&+ e^{-2ik(a-d)}\left[(1+\gamma)^2 e^{ipa} - (1-\gamma)^2 e^{-ipa}\right]\left[(1+\chi)^2 e^{iqa} - (1-\chi)^2 e^{-iqa}\right]
\end{aligned} \tag{B.48}$$

$$\begin{aligned}
F &= 2(1+\gamma)^2(1+\chi)^2 cos\left[a(p+q) - 2k(a-d)\right] \\
&+ 2(1-\gamma)^2(1-\chi)^2 cos\left[a(p+q) + 2k(a-d)\right] \\
&- 2(1+\gamma)^2(1-\chi)^2 cos\left[a(p-q) - 2k(a-d)\right] \\
&- 2(1-\gamma)^2(1+\chi)^2 cos\left[a(p-q) + 2k(a-d)\right]
\end{aligned} \tag{B.49}$$

To simplify the derivation, let:

$$\begin{aligned} \theta &= k(a-d) \\ M &= (1-\gamma^2)^2(1-\chi^2)^2 \\ N_1 &= (1+\gamma)^2(1+\chi)^2 \\ N_2 &= (1-\gamma)^2(1-\chi)^2 \\ N_3 &= (1+\gamma)^2(1-\chi)^2 \\ N_4 &= (1-\gamma)^2(1+\chi)^2 \end{aligned} \tag{B.50}$$

We then have for the $(D+E)$ term:

$$\begin{aligned} (D+E) &= 2M(N_1+N_2+N_3+N_4)cos2\theta(cos\,2aq - cos\,2ap - 1) \\ &- 2M\,[N_1 cos\,2(a(p+q)-\theta) + N_2 cos\,2(a(p+q)+\theta) \\ &+ N_3 cos\,2(a(p-q-\theta) + N_4 cos\,2(a(p-q)+\theta)] \\ &+ 4M sin\,2\theta\,[(N_1-N_2)cos\,a(p-q)sin\,a(p+q) + (N_3-N_4)cos\,a(p+q)sin\,a(p-q)] \end{aligned} \tag{B.51}$$

Putting it all together for the denominator of the transmission probability one has:

$$\begin{aligned} T_D &= 16^2\gamma^2\chi^2 + 64[(1-\gamma^2)^2\chi^2 sin^2 pa + (1-\chi^2)^2\gamma^2 sin^2 qa] \\ &+ 32(1-\gamma^2)^2(1-\chi^2)^2 sin^2(pa)sin^2(qa) \\ &+ 2M(N_1+N_2+N_3+N_4)cos\,2\theta(cos\,2aq - cos\,2ap - 1) \\ &- 2M\,[N_1 cos\,2(a(p+q)-\theta) + N_2 cos\,2(a(p+q)+\theta) \\ &+ N_3 cos\,2(a(p-q)-\theta) + N_4 cos2(a(p-q)+\theta)] \\ &+ 4M sin\,2\theta\,[(N_1-N_2)cos\,a(p-q)sin\,a(p+q) + (N_3-N_4)cos\,a(p+q)sin\,a(p-q)] \end{aligned} \tag{B.52}$$

B.2 Scattering Matrix of CPP Magnetic Multilayers

The interface resistance of two bilayers of (F/N/F/N) of the multilayered structure in CPP configuration can be modelled as a double square potential barrier whose individual barrier depends on the alignment of the magnetizations in adjacent F layers. We assume independent propagation of two spin channels with absolute spin direction (+) and (-) and relative direction

(↑), (↓) - with respect to the magnetization moment in the F layer) in the multilayer, and each channel has its own S matrix. The potential barriers are assumed to be spin-dependent: In the interface between $(F(\uparrow)/N)$, we have $V_\uparrow$, while in the interface between $(F(\downarrow)/N)$, we have $V_\downarrow$; and $V_\uparrow < V_\downarrow$.

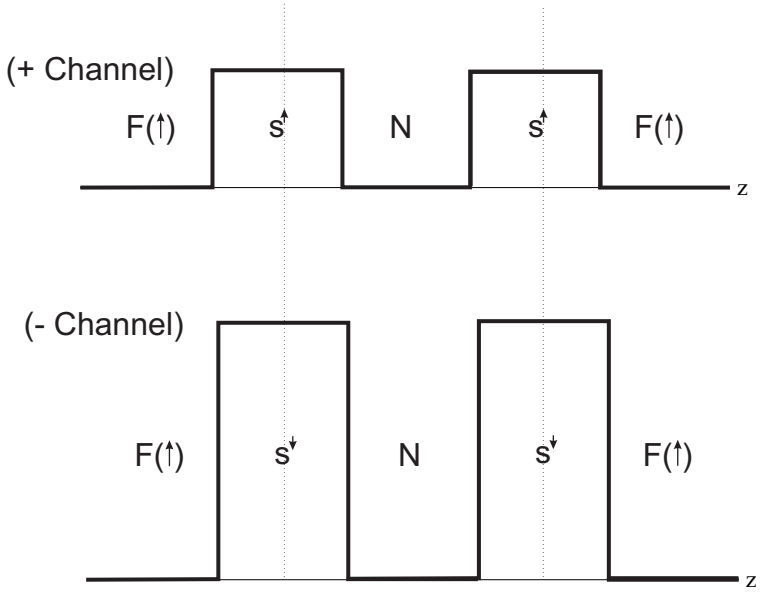

Figure B.2: Double potential barrier for P case.

The wavevector associated with each type of potential barrier is:

$$\begin{aligned} k &= \frac{\sqrt{2mE}}{\hbar} \\ k_\uparrow &= \frac{\sqrt{2m(E - V_\uparrow)}}{\hbar} \\ k_\downarrow &= \frac{\sqrt{2m(E - V_\downarrow)}}{\hbar} \\ \alpha &= \frac{k}{k_\uparrow} \\ \beta &= \frac{k}{k_\downarrow} \end{aligned} \tag{B.53}$$

The transmission coefficient is related to the conductance G by: $G = \frac{e^2}{\hbar}T$; and using to

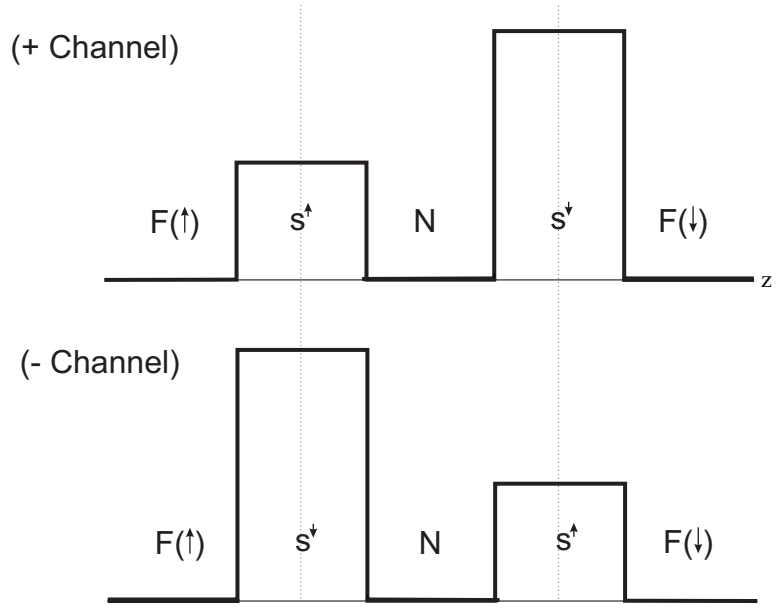

Figure B.3: Double potential barrier for AP case.

independent spin channels, the total conductance G_T is :

$$\begin{aligned} G_T &= G(+) + G(-) \\ \frac{e^2}{h}T &= \frac{e^2}{h}T(+) + \frac{e^2}{h}T(-) \end{aligned} \tag{B.54}$$

Hence: $T = T(+) + T(-)$ is the equivalent transmission coefficient of the 2 channels through the double square potential barrier.

B.2.1 Incoherent Transport

B.2.1.1 Anti-Parallel

In Anti-parallel configuration we have $(F(\uparrow)/N/F(\downarrow)/N)$, and thus the scattering matrix for each spin channel is:

$$\begin{aligned} S_{AP}(+) &= S(\uparrow) \otimes S(\downarrow) \\ S_{AP}(-) &= S(\downarrow) \otimes S(\uparrow) \end{aligned} \tag{B.55}$$

Using (B.40), the transmission coefficient for each spin channel is:

$$T_{AP}(+) = \frac{16^2\alpha^2\beta^2}{16^2\alpha^2\beta^2 + 64\left[(1-\alpha^2)^2\beta^2 sin^2 k_\uparrow a + (1-\beta^2)^2\alpha^2 sin^2 k_\downarrow a\right]} \tag{B.56}$$

B.2.1.2 Parallel

In Parallel configuration we have $(F(\uparrow)/N/F(\uparrow)/N)$, and thus the scattering matrix for each spin channel is:

$$\begin{aligned} S_P(+) &= S(\uparrow) \otimes S(\uparrow) \\ S_P(-) &= S(\downarrow) \otimes S(\downarrow) \end{aligned} \tag{B.57}$$

$$T_P(+) = \frac{16^2\alpha^4}{16^2\alpha^4 + 128(1-\alpha^2)^2\alpha^2(sin^2k_\uparrow a)} \tag{B.58}$$

$$T_P(-) = \frac{16^2\beta^4}{16^2\beta^4 + 128(1-\beta^2)^2\beta^2(sin^2k_\downarrow a)} \tag{B.59}$$

Total transmission for P case : $T_P = \frac{T_N(P)}{T_D(P)} = T_P(+) + T_P(-)$

$$T_N(P) = 2 \times (16\alpha\beta)^4 + 128 \times (16\alpha\beta)^2 \left[\left(\alpha(1-\beta^2)sin(k_\downarrow a)\right)^2 + \left(\beta(1-\alpha^2)(sin(k_\uparrow a))^2\right)\right] \tag{B.60}$$

$$\begin{aligned} T_D(P) &= (16\alpha\beta)^4 + 128 \times (16\alpha\beta)^2 \left[\left(\alpha(1-\beta^2)sin(k_\downarrow a)\right)^2 + \left(\beta(1-\alpha^2)(sin(k_\uparrow a))^2\right]\right. \\ &+ \left(128\alpha\beta(1-\alpha^2)(1-\beta^2)sin(k_\downarrow a)sin(k_\uparrow a)\right)^2 \end{aligned} \tag{B.61}$$

B.2.1.3 Comparison Between T_P and T_{AP} In Incoherent Transport

We are interested in the ratio:

$$\frac{T_{AP}}{T_P} = \frac{A_N}{A_D} \tag{B.62}$$

Letting: $\Lambda = 64\left(\left(\alpha(1-\beta^2)sin(k_\downarrow a)\right)^2 + \left(\beta(1-\alpha^2)sin(k_\uparrow a)\right)^2\right)$
and $\Delta^2 = \left(128\alpha\beta(1-\alpha^2)(1-\beta^2)sin(k_\downarrow a)sin(k_\uparrow a)\right)^2$
Substituting relevant expressions for T_{AP} and T_P from above, we have the following:

$$A_N = (16\alpha\beta)^4 + 2 \times (16\alpha\beta)^2\Lambda + \Delta^2 \tag{B.63}$$

$$A_D = \left[(16\alpha\beta)^2 + \Lambda\right]^2 \tag{B.64}$$

We then have:

$$\frac{T_{AP}}{T_P} = \frac{A_N}{A_D} = \frac{(16\alpha\beta)^4 + 2\times(16\alpha\beta)^2\Lambda + \Delta^2}{\left[(16\alpha\beta)^2 + \Lambda\right]^2} \tag{B.65}$$

$$\frac{T_{AP}}{T_P} = \frac{\left[(16\alpha\beta)^2 + \Lambda\right]^2 - (\Lambda^2 - \Delta^2)}{\left[(16\alpha\beta)^2 + \Lambda\right]^2} = 1 - \frac{(\Lambda^2 - \Delta^2)}{\left[(16\alpha\beta)^2 + \Lambda\right]^2} = 1 - \gamma^2 \tag{B.66}$$

The explicit expression for γ is:

$$\gamma = \frac{\sqrt{\Lambda^2 - \Delta^2}}{((16\alpha\beta)^2 + \Lambda)} = \frac{64\left(\left(\alpha(1-\beta^2)sin(k_\downarrow a)\right)^2 - \left(\beta(1-\alpha^2)sin(k_\uparrow a)\right)^2\right)}{((16\alpha\beta)^2 + \Lambda)} \tag{B.67}$$

Considering the factor: $\frac{T\uparrow - T\downarrow}{T\uparrow + T\downarrow}$ where $T\uparrow$ and $T\downarrow$ are the transmission probabilities through the double square potential barrier with potential $V\uparrow$ and $V\downarrow$, respectively (just like in the P case above). Here in this case we have:

$$T\uparrow = T_P(+) \tag{B.68}$$

$$T\downarrow = T_P(-) \tag{B.69}$$

$$\frac{T\uparrow - T\downarrow}{T\uparrow + T\downarrow} = \frac{T_P(+) - T_P(-)}{T_P(+) + T_P(-)} \tag{B.70}$$

B.2.1.4 Parallel

In P case, each spin channel experiences its same potential throughout the multilayer, hence we have (the numerator of the transmission probability T is denoted T_{PN} and the denominator T_{PD}, as above):

For (+) channel:

$$\begin{aligned} M &= (1-\alpha^2)^4 \\ N_1 &= (1+\alpha)^4 \\ N_2 &= (1-\alpha)^4 \\ N_3 = N_4 &= (1-\alpha^2)^2 \end{aligned} \tag{B.71}$$

Substituting the above into the general expression for T in coherent transport with $p = q = k\uparrow$ and $\gamma = \chi = \alpha$, one has:

$$T_{PN}(+) = 16^2\alpha^4 \tag{B.72}$$

$$\begin{aligned} T_{PD}(+) &= 128\alpha^4 + 32\left[2\alpha^2 + (1-\alpha^2)^2 sin^2 k_\uparrow a\right]^2 \\ &+ 4(1-\alpha^2)^4(1+\alpha^2)\left[4\alpha(cos\,2(ak_\uparrow - \theta) - cos\,2(ak_\uparrow + \theta)) - cos\,2\theta\right] \\ &- 2(1-\alpha^2)^4\left[(1+\alpha)^4 cos(4ak_\uparrow - 2\theta) + (1-\alpha)^4 cos(4ak_\uparrow + 2\theta)\right] \end{aligned} \tag{B.73}$$

$$T_{PD}(+) = 128\alpha^4 + 32\left[2\alpha^2 + (1-\alpha^2)^2 sin^2 k_\uparrow a\right]^2 + F_\alpha \tag{B.74}$$

(All explicit θ-dependence has been absorbed into F_α)

$$T_P(+) = \frac{16^2\alpha^4}{128\alpha^4 + 32\left[2\alpha^2 + (1-\alpha^2)^2 sin^2 k_\uparrow a\right]^2 + F_\alpha} \tag{B.75}$$

For (-) channel:

$$\begin{aligned} M &= (1-\beta^2)^4 \\ N_1 &= (1+\beta)^4 \\ N_2 &= (1-\beta)^4 \\ N_3 = N_4 &= (1-\beta^2)^2 \end{aligned} \tag{B.76}$$

Substituting the above into the general expression for T in coherent transport with $p = q = k\downarrow$ and $\gamma = \chi = \beta$, one has:

$$T_{PN}(-) = 16^2\beta^4 \tag{B.77}$$

$$\begin{aligned} T_{PD}(-) &= 128\beta^4 + 32\left[2\beta^2 + (1-\beta^2)^2 sin^2 k_\downarrow a\right]^2 \\ &+ 4(1-\beta^2)^4(1+\beta^2)\left[4\beta(cos2(ak_\downarrow - \theta) - cos\,2(ak_\downarrow + \theta)) - cos\,2\theta\right] \\ &- 2(1-\beta^2)^4\left[(1+\beta)^4 cos(4ak_\downarrow - 2\theta) + (1-\beta)^4 cos(4ak_\downarrow + 2\theta)\right] \end{aligned} \tag{B.78}$$

$$T_{PD}(-) = 128\beta^4 + 32\left[2\beta^2 + (1-\beta^2)^2 sin^2 k_\downarrow a\right]^2 + F_\beta \tag{B.79}$$

(All explicit θ-dependence has been absorbed into F_β)

$$T_P(-) = \frac{16^2\beta^4}{128\beta^4 + 32\left[2\beta^2 + (1-\beta^2)^2 sin^2 k_\downarrow a\right]^2 + F_\beta} \tag{B.80}$$

With

$$\begin{aligned} \eta^2 &= \left[2\alpha^2 + (1-\alpha^2)^2 sin^2 k_\uparrow a\right]^2 \\ \kappa^2 &= \left[2\beta^2 + (1-\beta^2)^2 sin^2 k_\downarrow a\right]^2 \end{aligned} \tag{B.81}$$

Using the obtained expressions for $T_P(+)$ and $T_P(-)$ above, one has:

$$\frac{T\uparrow - T\downarrow}{T\uparrow + T\downarrow} = \frac{64\left(\left(\alpha(1-\beta^2)sin(k_\downarrow a)\right)^2 - \left(\beta(1-\alpha^2)sin(k_\uparrow a)\right)^2\right)}{\left((16\alpha\beta)^2 + 64\left(\left(\alpha(1-\beta^2)sin(k_\downarrow a)\right)^2 + \left(\beta(1-\alpha^2)sin(k_\uparrow a)\right)^2\right)\right)} \tag{B.82}$$

Comparing (B.67), (B.82), and the expression for Λ above, it is obvious that:

$$\gamma = \frac{T\uparrow - T\downarrow}{T\uparrow + T\downarrow} \tag{B.83}$$

In general, the resistance R is related to the transmission probability T as:

$$R = \frac{1}{G} = \left(\frac{h}{e^2}\right)\frac{1}{T} \tag{B.84}$$

Therefore:

$$\gamma = \frac{T\uparrow - T\downarrow}{T\uparrow + T\downarrow} = \frac{R\downarrow - R\uparrow}{R\uparrow + R\downarrow} \tag{B.85}$$

Since the double square potential barrier is a model for a (F/N) interface, the interface resistance R_P and R_{AP} are explicitly related to T_P and T_{AP}:

$$R_{P/AP} = \frac{1}{G_{P/AP}} = \left(\frac{h}{e^2}\right)\frac{1}{T_{P/AP}} \tag{B.86}$$

Therefore:

$$\frac{R_P}{R_{AP}} = \frac{G_{AP}}{G_P} = \frac{T_{AP}}{T_P} = 1 - \gamma^2 \tag{B.87}$$

This means the same as:

$$R_{AP} = \frac{R_P}{1 - \gamma^2} \tag{B.88}$$

Eq.(B.88) is exactly the stated relation $AR^*_{F/N} = \frac{AR_{F/N}}{1-\gamma^2}$ in the 2CSR Model, where γ in that model is the interfacial spin asymmetry coefficient, which is defined in the same way as (B.85).

This shows that the 2CSR model is fundamentally an incoherent transport phenomenon.

B.2.2 Coherent Transport

B.2.2.1 Anti-Parallel

For AP case, the expression for transmission probability through the double square barrier is identical for (+) and (-) spin channel, and identical to that given above in the general case for coherent transport with $\gamma = \alpha$, $p = k_\uparrow$, $\chi = \beta$, and $q = k_\downarrow$:

$$T_{APN}(+) = T_{APN}(-) = (16\alpha\beta)^2 \tag{B.89}$$

$$\begin{aligned} T_{APD}(+) = T_{APD}(-) \quad &= \quad 16^2\alpha^2\beta^2 + 64[(1-\alpha^2)^2\beta^2 sin^2 k_\uparrow a + (1-\beta^2)^2\alpha^2 sin^2 k_\downarrow a] \\ &+ \quad 32(1-\alpha^2)^2(1-\beta^2)^2 sin^2(k_\uparrow a) sin^2(k_\downarrow a) \\ &+ \quad 2M(N_1 + N_2 + N_3 + N_4) cos 2\theta (cos\, 2ak_\downarrow - cos\, 2ak_\uparrow - 1) \\ &- \quad 2M\,[N_1 cos\, 2(a(k_\uparrow + k_\downarrow) - \theta) + N_2 cos\, 2(a(k_\uparrow + k_\downarrow) + \theta) \\ &+ \quad N_3 cos\, 2(a(k_\uparrow - k_\downarrow) - \theta) + N_4 cos\, 2(a(k_\uparrow - k_\downarrow) + \theta)] \\ &+ \quad 4M sin\, 2\theta\,[(N_1 - N_2) cos\, a(k_\uparrow - k_\downarrow) sin\, a(k_\uparrow + k_\downarrow) \\ &+ \quad (N_3 - N_4) cos\, a(k_\uparrow + k_\downarrow) sin\, a(k_\uparrow - k_\downarrow)] \end{aligned} \tag{B.90}$$

with M, N_1, N_2, N_3, N_4, and θ defined as in the general case ($\gamma = \alpha$, $\chi = \beta$)

$$\begin{aligned}
\theta &= k(a-d) \\
M &= (1-\alpha^2)^2(1-\beta^2)^2 \\
N_1 &= (1+\alpha)^2(1+\beta)^2 \\
N_2 &= (1-\alpha)^2(1-\beta)^2 \\
N_3 &= (1+\alpha)^2(1-\beta)^2 \\
N_4 &= (1-\alpha)^2(1+\beta)^2
\end{aligned}$$

$$\begin{aligned}
T_{APD}(+) = T_{APD}(-) &= 16^2\alpha^2\beta^2 + \Lambda \\
&+ 32(1-\alpha^2)^2(1-\beta^2)^2 sin^2(k_\uparrow a) sin^2(k_\downarrow a) \\
&+ F_{\alpha\beta}
\end{aligned}$$

($F_{\alpha\beta}$ is the term that absorbs all θ dependence in the above expression and Λ has been defined in the previous section)

The total transmission probability is:

$$\begin{aligned}
T_{AP} &= 2T_{AP}(+) = 2T_{AP}(-) \\
&= \frac{2 \times (16\alpha\beta)^2}{16^2\alpha^2\beta^2 + \Lambda + 32((1-\alpha^2)(1-\beta^2) sin(k_\uparrow a) sin(k_\downarrow a))^2 + F_{\alpha\beta}}
\end{aligned}$$

$$T_{AP} = \frac{2 \times (16\alpha\beta)^2}{(16\alpha\beta)^2 + \Lambda + \frac{\Delta^2}{512(\alpha\beta)^2} + F_{\alpha\beta}} \tag{B.91}$$

The equivalent transmission probability for P case in coherent transport is:

$$T_P = T_P(+) + T_P(-) \tag{B.92}$$

$$T_P = \frac{16^2\alpha^4}{[128\alpha^4 + 32\eta^2]} + \frac{16^2\beta^4}{[128\beta^4 + 32\kappa^2]} \tag{B.93}$$

$$T_P = \frac{\left[(16\alpha\beta)^2 + \Lambda)^2 + (\Lambda^2 - v\Delta^2) + (16\alpha\beta)^4 + 16^2(\alpha^4 F_\beta + \beta^4 F_\alpha)\right]}{\left[\left[(16\alpha\beta)^2 + \Lambda\right]^2 + \left[\Lambda + \frac{\Delta^2}{512(\alpha\beta)^2}\right]^2 + F_\alpha F_\beta + 32[F_\beta(\eta^2 + 4\alpha^4) + F_\alpha(\kappa^2 + 4\beta^4)]\right]} \tag{B.94}$$

B.2.2.2 Comparison Between T_P and T_{AP} In Coherent Transport

Considering the quantity γ, defined in the same way as in incoherent transport:

$$\gamma = \frac{T\uparrow - vT\downarrow}{T\uparrow + T\downarrow} = \frac{T_P(+) - T_P(-)}{T_P(+) + T_P(-)} \tag{B.95}$$

Substituting (B.75) and (B.80) into (B.95):

$$\gamma = \frac{32(16^2)(\alpha^4\kappa^2 - \beta^4\eta^2) + 16^2(\alpha^4 F_\beta - \beta^4 F_\alpha)}{(16\alpha\beta)^4 + 32(16^2)(\alpha^4\kappa^2 + \beta^4\eta^2) + 16^2(\alpha^4 F_\beta + \beta^4 F_\alpha)} \tag{B.96}$$

$$\gamma = \frac{2\sqrt{\Lambda^2 - \Delta^2}\left[(16\alpha\beta)^2 + \Lambda\right] + 16^2(\alpha^4 F_\beta - \beta^4 F_\alpha)}{[(16\alpha\beta)^2 + \Lambda)^2 + (\Lambda^2 - \Delta^2) + (16\alpha\beta)^4 + 16^2(\alpha^4 F_\beta + \beta^4 F_\alpha)]} \tag{B.97}$$

Again, we are interested in the ratio: $\frac{R_P}{R_{AP}} = \frac{T_{AP}}{T_P}$. From (B.91) and (B.94), one has:

$$\begin{aligned}\frac{T_{AP}}{T_P} &= \frac{\Gamma_N}{\Gamma_D} = \left[\frac{2 \times (16\alpha\beta)^2}{(16\alpha\beta)^2 + \Lambda + \frac{\Delta^2}{512(\alpha\beta)^2} + F_{\alpha\beta}}\right] \\ &\times \left\{\frac{\left[(16\alpha\beta)^2 + \Lambda)^2 + (\Lambda^2 - \Delta^2) + (16\alpha\beta)^4 + 16^2(\alpha^4 F_\beta + \beta^4 F_\alpha)\right]}{\left\{[(16\alpha\beta)^2 + \Lambda]^2 + \left[\Lambda + \frac{\Delta^2}{512(\alpha\beta)^2}\right]^2 + F_\alpha F_\beta + 32[F_\beta(\eta^2 + 4\alpha^4) + F_\alpha(\kappa^2 + 4\beta^4)]\right\}}\right\}^{-1}\end{aligned} \tag{B.98}$$

$$= \frac{2(16\alpha\beta)^2\left\{[(16\alpha\beta)^2 + \Lambda]^2 + \left[\Lambda + \frac{\Delta^2}{512(\alpha\beta)^2}\right]^2 + F_\alpha F_\beta + 32[F_\beta(\eta^2 + 4\alpha^4) + F_\alpha(\kappa^2 + 4\beta^4)]\right\}}{\left[(16\alpha\beta)^2 + \Lambda + \frac{\Delta^2}{512(\alpha\beta)^2} + F_{\alpha\beta}\right]\{[(16\alpha\beta)^2 + \Lambda]^2 + (\Lambda^2 - \Delta^2) + (16\alpha\beta)^4 + 16^2(\alpha^4 F_\beta + \beta^4 F_\alpha)\}} \tag{B.99}$$

Using (B.97), (B.99), it can be shown that, for coherent transport:

$$\frac{R_P}{R_{AP}} = \frac{T_{AP}}{T_P} \neq 1 - \gamma^2 \tag{B.100}$$

This shows that the relation:

$$\frac{R_P}{1 - \gamma^2} = R_{AP} \tag{B.101}$$

does not hold in coherent transport.

Afterword

I have had a very fruitful time in CMS group - learning not only a lot of new physics but also a way of studying and analyzing the problems, and a way of attempting to understand the big picture with the consistent physics behind it. There are still a lot of questions remaining, but overall, the whole journey has been rather satisfying. Throughout my project, everytime a new calculation's result is obtained, the problem gets redefined as the result turns out to be different from what we expected. And through it all, I am deeply grateful to many individuals: to Zhe, my direct supervisor, for teaching me the calculation methods using LMTOs, the transport calculations, for guiding me through the interpretation of results, and for going through my final report carefully; to Paul, for his many new and often intriguing ideas that usually took me to a different direction of searching for physical answers; to Geert, for his impressive patience in explaining and making difficult physics more understandable to me. To Anton, for entertaining my questions about the codes, the physics of LMTOs and other physics, and to answer all of them extensively. To Taher, for spending time meticulously discussing and checking through my maths in the coherent/incoherent transport chapter. To Rien, for taking interest in my problems and offering a way of explaining them convincingly. To Yi, for answering any inpromptu physics questions I might have in the office. To Diana, for all the pleasant and difficult time that we shared. To many others in the group that I have come to know and appreciate. To H. Wormeester from the PIN group, for explaining to me twice on experimental characterizations and the basics of x-ray diffraction scans. To G. Koster from the IMS group, for receiving me unexpectedly and explaining patiently to me different experimental characterizations done in his group on his multilayer samples. To S. F. Lee (previously from the MSU group) for providing me with his PhD thesis for my reference. And most of all, to my loyal companion, C.C., for his love and support, without which, none of this would have been possible.

Bibliography

[1] S. F. Lee, Q. Yang, P. Holody, R. Loloee, J. H. Hetherington, S. Mahmood, B. Ikegami, K. Vigen, L. L. Henry, P. A. Schroeder, Jr. W. P. Pratt, and J. Bass. *Physical Review B*, 52:15426–15441, 1995. 1, 22, 23, 28, 29

[2] W. P. Pratt Jr., S. F. Lee, P. Holody, Q. Yang, R. Loloee, J. Bass, and P. A. Schroeder. *Journal of Magnetism and Magnetic Materials*, 126:406–409, 1993. 1, 21, 28, 29, 39, 54, 55, 56

[3] J. Kubler. *Theory of Itinerant Electron Magnetism*. Oxford Science Publications, 2000. 3

[4] V. Drchal I. Turek, J. Kudrnovsk, M. Sob, and P. Weinberger. *Electronic Structure of Disordered Alloys, Surfaces and Interfaces*. Springer, 1997. 6

[5] P. A. Khomyakov and G. Brocks. *Physical Review B*, 70:195402, 2004. 12, 15

[6] G. H. O. Daalderop, P. J. Kelly, and M. F. H. Schuurmans. *Physical Review B*, 41:11919–11937, 1990. 19

[7] S. F. Lee, W. P. Pratt Jr., Q. Yang, P. Holody, R. Loloee, P. A. Schroeder, and J. Bass. *Journal of Magnetism and Magnetic Materials*, 118:L1–L5, 1993. 21

[8] D. L. Edmunds, W. P. Pratt Jr., and J. A. Rowlands. *Review of Scientific Instruments*, 51:1516–1522, 1980. 23

[9] J. Bass and W. P. Pratt Jr. *Journal of Physics: Condensed Matter*, 19:183201, 2007. 25

[10] S. F. Lee. *PhD. Thesis*. PhD thesis, Michigan State University, 1994. 24, 26, 27, 56

[11] S. Pizzini, F. Baudelet, A. Fontaine, M Galtier, D. Renard, and C. Marlire. *Physical Review B*, 47:9754, 1993. 27

[12] J. Bass and W. P. Pratt Jr. *Journal of Magnetism and Magnetic Materials*, 200:274–289, 1999. 29, 30, 54

[13] B. Didier, M. A. Howson, B. J. Hickey, N. Wiser S. Shatz, E. Y. Tsymbal, and D. G. Pettifor. *Physical Review Letters*, 85:1314–1317, 2000. 30, 32

[14] Didier Bozec, M. A. Howson, S. Shartz B. J. Hickey, N. Wiser, E. Y. Tsymbal, and D. G. Pettifor. *Physical Review Letters*, 85:1314–1317, 2000. 31

[15] K. Eid, D. Portner, J. A. Borchers, R. Loloee, M. Al-Haj Darwish, R. D. Slater M. Tsoi, K. V. ODonovan, H. Kurt, Jr. W. P. Pratt, and J. Bass. *Physical Review B*, 65:054424, 2002. 32, 33

[16] T. Valet and A. Fert. *Physical Review B*, 48:7099–7113, 1993. 32

[17] Anton A. Starikov, Paul J. Kelly, Arne Brataas, Yaroslav Tserkovnyak, and Gerrit E. W. Bauer. *Physical Review Letters*, 105:236601, 2010. 42, 47

[18] P. A. Schroeder et al. *Materials Research Society Symposium Proceedings*, 47:313, 1993. 52

[19] Y. Liu, A. A. Starikov, Z. Yuan, and P. J. Kelly. *Physical Review B*, 84:014412, 2011. 55, 56

[20] A. G. Guy and J. J. Hren. *Elements of Physical Metallurgy*. Addison-Wesley, 1974. 59

[21] J. A. C. Bland and B. Heinrich. *Ultrathin Magnetic Structure III: Fundamentals of Nanomagnetism*. Springer, 2005. 60

[22] S. Mitchell and Prez-Ramrez J. *X-ray diffraction exercises*. Institute for Chemical and Bioengineering, ETH Zurich, Presentation. 61, 62

[23] P. A. Mello and N. Kumar. *Quantum Transport in Mesoscopic Systems: Complexity and Statistical Fluctuations*. Oxford University Press, 2004. 68

[24] S. Datta. *Electronic Transport in Mesoscopic Systems*. Cambridge University Press, 1997. 70